Geomech. Geophys. Geo-energ. Geo-resour. (2023) 9:29
https://doi.org/10.1007/s40948-023-00546-y

ORIGINAL ARTICLE

Numerical study on fracture control blasting using air–water coupling

Xudong Li · Kewei Liu · Tao Qiu · Yanyan Sha · Jiacai Yang · Ruitao Song

Received: 30 September 2022 / Accepted: 3 December 2022

Abstract Fracture control blasting produces rock fractures in the desired direction, which is significant for the stability of excavation structures in rock engineering. The present study proposes a new method of fracture control blasting using air–water coupling. This method utilizes the difference of explosion stress transfer between air and water, which guides the explosion energy consumption in fracturing rock on water-coupling side, i.e. rock in the excavation zone, and thus the rock in the excavation zone is properly fragmented, and the reserved rock is well protected from damage. Based on the plane strain assumption, the transmission and propagation of explosion stress in the excavation and reserved rock with this method are first theoretically analyzed. Then, fracture control blasting using air–water coupling is numerically studied utilizing the LS-DYNA program. The numerical model is first developed and calibrated in the simulation with the laboratory-scale air-coupling and water-coupling blasting tests. Then, the successive processes of pressure attenuation, fracture evolution and energy consumption under air–water coupling blasting are numerically investigated. Thereafter, the effects of the air–water ratio and decoupling ratio on the performance of fracture control are numerically investigated. The theoretical and numerical results show that good performance of fracture control can be obtained using air–water coupling blasting.

Article Highlights

- A new method of fracture control blasting using air–water coupling is proposed
- The new method utilizes the difference in stress transfer between air and water
- Good performance of fracture control is achieved under air–water coupling blasting

Keywords Fracture control blasting · Air–water coupling · Stress transmission · Crack evolution · Numerical simulation

1 Introduction

Drilling and blasting is the most commonly used excavation method in mining and civil engineering owing to its low cost and high efficiency. (An et al. 2017; Himanshu et al. 2022; Li et al. 2022b; Sun et al. 2022; Yan et al. 2015; Yi et al. 2017). However, lots of undesirable fractures in the remaining rock are

X. Li · K. Liu (✉) · T. Qiu · J. Yang · R. Song
School of Resources and Safety Engineering, Central South University, Changsha 410083, China
e-mail: kewei_liu@csu.edu.cn

Y. Sha
Department of Mechanical and Structural Engineering and Materials Science, University of Stavanger, 4021 Stavanger, Norway

Published online: 14 March 2023

induced by blast loading, which raises safety issues and increases the costs of support (Li et al. 2022a; Martino and Chandler 2004; Verma et al. 2018; Wang et al. 2022; Yang et al. 2022; Zou 2017). To protect the wall rock from damaging or even destructing under blast loading, controlled blasting such as smooth blasting is widely used. Unfortunately, since the explosion energy is well-distributed radially along the borehole wall in conventional controlled blasting, the rock mass beyond the excavation boundary may not be well protected (Kirsch 1898). Under this condition, the fracture control blasting technique that controls the initiation and propagation of blast-induced cracks and generates smooth excavation boundaries with intact surrounding rock, needs to be employed and further developed in rock engineering.

Fracture control blasting aims to promote fracture development in the desired direction and reduce cracks in the remaining rock. In a pioneering study, Foster (1905) first proposed the concept of fracture control in blasting using a notched borehole to promote fracture growth in the desired direction. However, this technology was not successfully implemented due to the lack of a theoretical base, experimental verification and relevant construction techniques. After that, to control the initiation, propagation and interpenetration of fracture in perimeter excavation, smooth blasting was introduced in the early 1950s (Langefors et al. 1963). Smooth blasting is an extraordinary technique that inaugurated a new era in contour excavation using drilling and blasting. In smooth blasting, numerous closely spaced boreholes are lightly loaded with well-distributed charges and simultaneously detonated to create a smooth surface and remain relatively intact host rock. Sometimes, unloaded or dummy holes between the loaded holes are employed in smooth blasting to guide the fracture extension to improve the performance of fracture control (Li et al. 2017; Mckown 1986; Nakagawa et al. 1982). Moreover, some other controlled blasting techniques, including presplit blasting and fracture control blasting, were developed based on smooth blasting (Singh et al. 2014; Yi et al. 2017). Among these improved controlled blasting techniques, the fracture control blasting technique that commonly uses a special borehole and cartridge has the great advantage of directionally controlling the propagation of blast-induced fracture, which has broad application prospects in contour excavation.

In the early stage of the development of fracture control blasting technology, three attractive fracture control blasting techniques using notched borehole, slotted cartridge and shaped charge were widely employed in various types of rock engineering such as tunnelling (Shu et al. 2013, 2014; Thompson et al. 1979), mining (Hustrulid and Bullock 2001) and rock excavation in quarries (Sanchidrián et al. 2000; Tsoutrelis et al. 1997). The fracture control blasting using a notched borehole was introduced by Langefors et al. (1963). Notching increases the stress concentration on the borehole wall and thus reduces the explosion pressure required for crack initiation, and it permits control of the initiation location for radial fractures which produce the specified fracture surface (Cho et al. 2008; Dally and Fourhey 1977; Ma and An 2008; Mckown 1986). However, notching the blasthole is an additional step after drilling, and the notching tools developed to date show low efficiency in hard rock. Fracture control blasting using a slotted cartridge was invented by Fourney et al. (1978). The essence of slotted cartridge blasting is to open slots in a specified direction on the explosive holder. This slotted holder, under the combination of explosion stress and quasi-static pressure of explosion gas, produces highly concentrated stresses on the borehole wall at the slot locations, and these concentrated stresses initiate cracks that propagate outward to form the controlled fracture plane (Fourney et al. 1978, 1983; Li et al. 2021b; Ma and An 2008; Wang 2017). In this way, the initiation and propagation of blast-induced fractures are controlled by aligning the specified direction. However, this technique of fracture control blasting needs a slotted holder with high strength for guiding and concentrating the explosion products generated in explosive burning. The production of the slotted cartridge is costly, which significantly increases the costs of rock blasting. The phenomenon of shaped charge jet was first observed in the 1790s, and was extensively studied during World War II (Jiang 2010; Liu et al. 2019a). In 1983, the effect of shaped charge jet penetration was introduced in rock blasting with a linear-shaped charge to control the growth of rock fracture by Bjarnholt et al. (1983). When the linear-shaped charge is ignited, the shaped charge jet penetration immediately acts on the borehole wall in the direction of the open slot of the shaped charge, and thus radial cracks initiate and propagate outwards in the desired direction,

ultimately creating a smooth fracture surface (Luo and Shen 2006; Yin et al. 2021). To ensure the formation of shaped charge jet, an explosive with a high velocity of detonation (VOD) is needed. However, the production of shaped charge is costly too, and the VODs of explosives are commonly used in controlled blasting, such as emulsion explosives, are relatively low, restricting the application of shaped charge blasting in perimeter excavation.

In recent years, some new fracture control blasting methods were proposed and tested to improve the performance of fracture control blasting. For example, two fracture control blasting methods were suggested by Nakamura et al. (1992), Nakamura (1999), including the guide hole method which utilizes a circular hole with notches and the charge holder method with two wedge-shaped air cavities to achieve crack propagation control. Model experiments using these two fracture control blasting methods showed that these methods effectively control the orientation of fracture extension and drive the controlled cracks to greater distances. Fracture control blasting using a combined notched borehole and time sequence control was proposed by Li et al. (2021a), and it was numerically demonstrated that the quality of the excavation profile could be ensured with low construction costs when using this technique. Apart from these, new fracture control blasting techniques such as Bilateral Cumulative Tensile Explosion (He et al. 2003; Zhang et al. 2020), Elliptic Bipolar Linear Shaped Charge Blasting (Li 2013), Bilateral–Groove–Slot Shaped Charge Blasting (Yin et al. 2021), etc., were recently developed. However, a complicated combination of special boreholes and cartridges is generally used in these new-developed techniques, which greatly increases the procedure and costs of rock blasting. Therefore, efforts need to be further made to develop techniques or methods of controlled fracture blasting with easy operation and low cost.

The present study proposes a new method of fracture control blasting using two coupling mediums (air and water) with a traditional borehole and cartridge. First, the conception of air–water coupling blasting is introduced and based on plain strain and linear elastic assumptions, the principle of air–water coupling blasting is theoretically analyzed with the transmission and propagation of explosion stress. Then, a numerical model is developed and calibrated against the pressure variation and fracture network

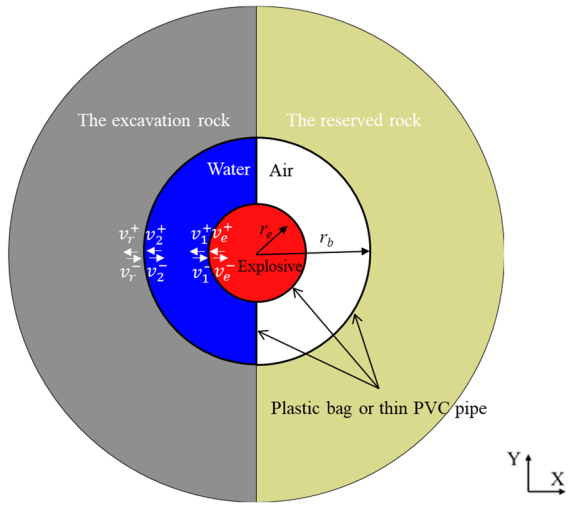

Fig. 1 Sketch of air–water coupling blasting

in laboratory-scale blasting tests, and this developed numerical model is used to model the new-proposed fracture control blasting in LS-DYNA. Through the simulation, the pressure attenuation, fracture evolution and energy consumption during air–water coupling blasting are studied. At last, the effects of the air–water ratio and decoupling coefficient on fracture control performance are investigated. According to the theoretical and numerical results, the fracture evolution mechanisms under the new-introduced fracture control blasting are revealed, and the implications of current findings for practical blasting are discussed. This study provides a new perspective concerning fracture control using drilling and blasting.

2 Principle of air–water coupling blasting

2.1 Air–water coupling blasting

In fracture control blasting using an air–water coupling, the air is filled between the central charge and borehole wall as a buffer layer on the reserved rock side. In contrast, the water is filled on the excavation rock side, as shown in Fig. 1. The separation of air and water can be easily achieved using a thin double-layer PVC pipe or double-layer cylindrical plastic bag with internal partitions.

It is well acknowledged that air is a low-density material with high compressibility and low wave

impedance. On the air-coupling side, part of the detonation energy is consumed in compressing air due to the high compressibility of air. Moreover, a large part of explosion stress waves reflects into the air at the air-rock interface due to the considerable difference in wave impedance between air and rock. As a result, explosion stress waves transfer into the rock on the air-coupling side with low efficiency, i.e., explosion energy transmitting through the air into rock mass is significantly decayed. Water has a much higher density and wave impedance than air, and it is generally characterized by incompressibility and low dissipation of stress wave transmission (Huang and Li 2015; Yan and Xu 2005; Yuan et al. 2019). During air–water coupling blasting, bubble pulsation may be produced within the borehole on the water-coupling side, and higher pressure of shock wave at the cartridge-water interface can be created than that in an infinite water area. Therefore, the water in the borehole can be taken as an energy transfer layer and transfers much more energy into rock than air, leading to denser and longer rock fractures in excavation rock than in reserved rock (Cui et al. 2010; Jang et al. 2018). This way, the rock on the excavation side is severely fragmented while the remaining rock mass experiences slight disturbance. Consequently, the rock in the excavation zone is efficiently removed, whereas the damage to the reserved rock is well controlled.

This method of fracture control blasting utilizes the difference in the transfer efficiency of explosion energy between air and water, which guides the explosion energy consumed in fracturing rock on the water-coupling side, i.e. the excavation rock. It has advantages such as easy operation and low cost since no special borehole and cartridge are used. At the same time, using air–water coupling benefits the control of vibration and dust during blasting.

2.2 Stress transfer in air–water coupling blasting

Based on Fig. 1, the successive process of stress transmission in air–water coupling blasting can be theoretically calculated using the Equivalent wave impedance method (Zhang et al. 1998). It should be noted that the plastic bag or PVC pipe is overlooked during the analysis of stress transmission since its low strength and very small thickness. In rock blasting, the materials near the interfaces between the explosive and coupling medium and between the coupling medium and rock are indeed not perfectly attached together before the detonation of explosive. But under the transient and intensive blast loading, the explosion products, coupling medium and rock are greatly compressed by explosion detonation so that the materials at the interfaces are squeezed together. Thus, in the current study, the velocities at interface-I (between explosive and coupling medium) and interface-II (between coupling medium and rock) can be assumed to be continuous. Simultaneously, the explosive, air, water and rock are all considered linear-elastic materials and the rock area is assumed to be infinite. Based on these assumptions, the relationship of stress σ_e and velocity v_e in explosive at the interface between explosive and coupling medium can be expressed as Li (2014):

$$\begin{cases} \sigma_e = \sigma_e^+ + \sigma_e^- = Z_e v_e^+ - Z_e v_e^- = Z_c v_1^+ - Z_c v_1^- \\ v_e = v_e^+ + v_e^- = v_1^+ + v_1^- \end{cases} \tag{1}$$

where Z_e and Z_c are the wave impedances of explosive and coupling medium, respectively. The Superscript "+" and "−" denote the outward spreading stress and velocity and reflected propagating stress and velocity, respectively. The subscript "1" and "2" denote interface I and II, respectively. Meanwhile, the stress σ_r and velocity v_r in rock at the interface of coupling medium and rock can be expressed as:

$$\begin{cases} \sigma_r = \sigma_r^+ + \sigma_r^- = Z_r v_r^+ - Z_r v_r^- = Z_c v_2^+ - Z_c v_2^- \\ v_r = v_r^+ + v_r^- = v_2^+ + v_2^- \end{cases} \tag{2}$$

where Z_r is the wave impedance of rock, and thus v_2 at the interface of coupling medium and rock can be expressed by:

$$\begin{cases} v_2^+ = 0.5 v_r + \sigma_r / 2 Z_c \\ v_2^- = 0.5 v_r - \sigma_r / 2 Z_c \end{cases} \tag{3}$$

Furthermore, the particle velocity in the coupling medium at the interface between the coupling medium and rock can be calculated by its counterpart at the interface between the explosive and coupling medium multiplying a phase factor and is expressed as:

$$\begin{cases} v_2^+ = v_1^+ e^{-i\alpha} \\ v_2^- = v_1^- e^{i\alpha} \end{cases} \tag{4}$$

where $e^{-i\alpha}$ and $e^{i\alpha}$ are the phase factors of transmitted explosion stress waves and reflected explosion stress waves in coupling material, respectively. $\alpha = 2\pi d_c / \lambda$, where d_c is the thickness of coupling

medium, λ is the wavelength of the detonation stress waves in coupling medium. This can be calculated by $\lambda = 1.5c_1 d_c^{0.5} w_c^{1/6} \times 10^{-3}$ and $\lambda = 7c_2 w_c^{0.5} K_d^{-0.45} \times 10^{-4}$ for air coupling and water coupling blasting, respectively, in which w_c is TNT equivalent weight of explosive, K_d is the decoupling ratio defined as the borehole radius r_b divided by the explosive radius r_e, c_1 and c_2 are the wave velocities in air and water, respectively (Henrych and Major 1979).

Submit Eqs. (3) and (4) to Eq. (1), the following expression can be obtained:

$$\begin{bmatrix} v_e \\ \sigma_e \end{bmatrix} = \begin{bmatrix} e^{i\alpha} & e^{-i\alpha} \\ Z_c e^{i\alpha} & -Z_c e^{-i\alpha} \end{bmatrix} \begin{bmatrix} v_2^+ \\ v_2^- \end{bmatrix} \tag{5}$$

And based on the Euler formula, Eq. (5) can be further written as:

$$\begin{bmatrix} v_e \\ \sigma_e \end{bmatrix} = \begin{bmatrix} \cos\alpha & \sin\alpha i / Z_c \\ Z_c \sin\alpha i & \cos\alpha \end{bmatrix} \begin{bmatrix} v_r \\ \sigma_r \end{bmatrix} \tag{6}$$

Herein, assuming the wave impedance for stress wave propagating through coupling medium into rock is Z_{c+r}, thus,

$$\begin{cases} \sigma_e = Z_e v_e^+ - Z_e v_e^- = Z_{c+r} v_{c+r} \\ v_e = v_e^+ + v_e^- = v_{c+r} \end{cases} \tag{7}$$

And Z_{c+r} can be easily derived as:

$$Z_{c+r} = \frac{Z_c i \sin\alpha + Z_r \cos\alpha}{\cos\alpha + i \sin\alpha Z_r / Z_c} \tag{8}$$

And finally, the stress transmission coefficient T_σ of explosion stress waves propagating from explosive to rock can be determined by $T_\sigma = 2Z_{c+r}/(Z_{c+r} + Z_e)$ and written as Li (2014):

$$T_\sigma = \frac{2\left(Z_c i \sin\alpha + Z_r \cos\alpha\right)}{\left(Z_r + Z_r\right)\cos\alpha + i \sin\alpha \left(Z_c^2 + Z_e Z_r\right)/Z_c} \tag{9}$$

According to Eqs. (1–9), with the physical and mechanical parameters given in the following Sect. 3 and borehole radius of 3.225 mm, the stress transmission coefficient vs. charge radius in the rock under air–water coupling blasting are plotted in Fig. 2. It can be seen that the stress transmission coefficient on water-coupling side is always higher than that on air-coupling side, meaning that the magnitude of explosion stress transmitted into the excavation rock is larger than that into the reserved rock. Moreover,

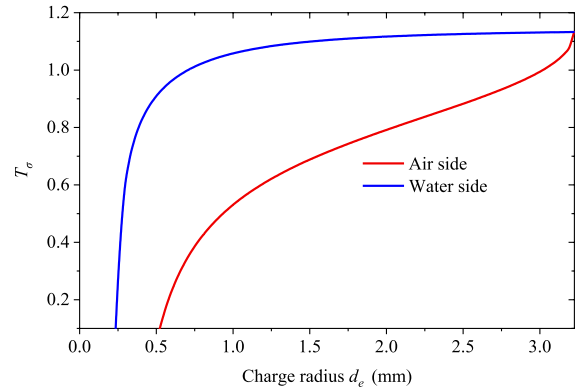

Fig. 2 Stress transmission under air–water coupling blasting

a smaller charge radius leads to a more considerable difference in stress transmission between the rock on the air and water side, implying that a small charge radius may be beneficial to the performance of fracture control under air–water coupling blasting.

2.3 Stress propagation in air–water coupling blasting

In general, the stress propagation induced by blasting is generalized as a problem of stress waves radiating from a pressurized hole, which can be solved using the Laplace transform and inversion transform. In the current theoretical analysis, the stress propagation generated by air–water coupling blasting in rock on the air-coupling and water-coupling side is approximately calculated as blasting using air-coupling and water-coupling, respectively. The governing equation for the propagation of explosion stress and the initial and boundary conditions are expressed as Miklowitz (1978):

$$\frac{\partial^2 u_d(r,t)}{\partial r^2} + \frac{\partial}{\partial r}\left(\frac{u_d(r,t)}{r}\right) = \frac{1}{c_p^2}\frac{\partial^2 u_d(r,t)}{\partial t^2}, (r > r_b, t > 0) \tag{10a}$$

$$u_d(r,0) = \frac{\partial u_d(r,0)}{\partial t} = 0, (r \geq r_b) \tag{10b}$$

$$\lim_{r\to\infty} u_d(r,t) = 0, (t \geq 0) \tag{10c}$$

$$\sigma_{dr}(r_b,t) = F(t) \tag{10d}$$

where $u_d(r,t)$ is the displacement potential function in cylindrical coordinates, r is the distance to the hole

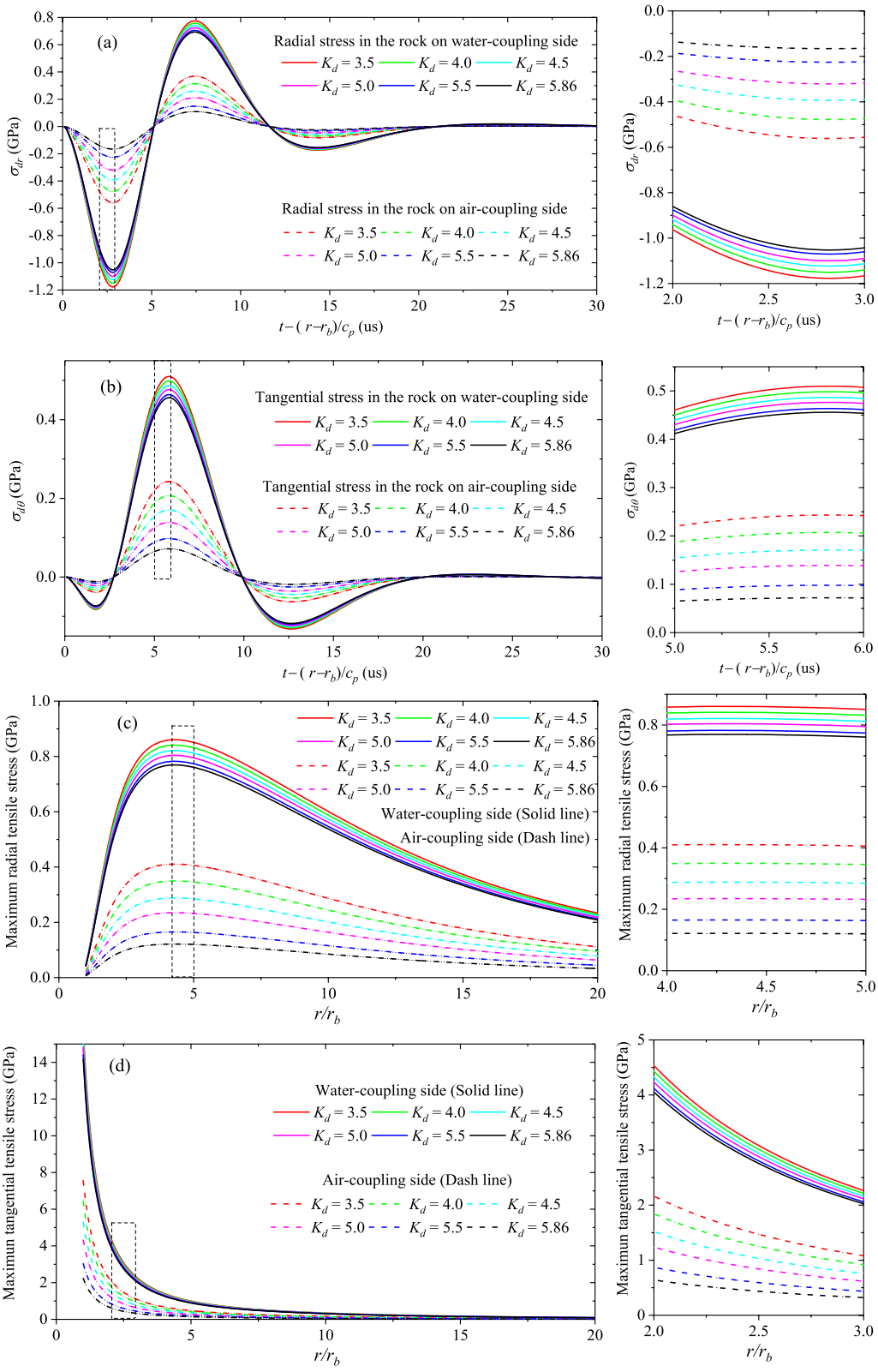
(a)
Radial stress in the rock on water-coupling side
K_d = 3.5 K_d = 4.0 K_d = 4.5
K_d = 5.0 K_d = 5.5 K_d = 5.86
Radial stress in the rock on air-coupling side
K_d = 3.5 K_d = 4.0 K_d = 4.5
K_d = 5.0 K_d = 5.5 K_d = 5.86
σ_{dr} (GPa)
$t-(r-r_b)/c_p$ (us)
(b)
Tangential stress in the rock on water-coupling side
Tangential stress in the rock on air-coupling side
$\sigma_{d\theta}$ (GPa)
(c)
Water-coupling side (Solid line)
Air-coupling side (Dash line)
Maximum radial tensile stress (GPa)
r/r_b
(d)
Maximun tangential tensile stress (GPa)

◂**Fig. 3** Time-history curves and their partially enlarged views of **a** radial stress and **b** tangential stress at $r=25$ mm and distribution curves of maximum tensile stress **c** in the radial direction and **d** in the tangential direction under air–water coupling blasting with different decoupling ratios

center, and t is the time. c_p is the P-wave velocity of rock. $F(t)$ is the blast loading applied on the borehole wall, and for the convenience of analytical solution, it is simplified as a triangular wave:

$$\begin{cases} T_\sigma P_{CJ} t/t_r, (0 \le t < t_r) \\ T_\sigma P_{CJ}(t_d - t)/(t_d - t_r), (t_r \le t \le t_d) \\ 0, (t > t_d) \end{cases} \tag{11}$$

where P_{CJ} is the Chapman–Jouget pressure, t_r (setting to 4 us) and t_d (setting to 10 us) is the rise time and duration of blast loading, respectively. According to the generalized Hooke's law, the components of the dynamic stress in radial direction σ_{dr} and tangential direction $\sigma_{d\theta}$ can be expressed as:

$$\sigma_{dr} = (\lambda + 2G)\frac{\partial^2 u_d(r,t)}{\partial r^2} + \frac{\lambda}{r}\frac{\partial u_d(r,t)}{\partial r} \tag{12a}$$

$$\sigma_{d\theta} = \lambda\frac{\partial^2 u_d(r,t)}{\partial r^2} + \frac{(\lambda + 2G)}{r}\frac{\partial u_d(r,t)}{\partial r} \tag{12b}$$

where λ and G are the Lame constants calculated by $\lambda = E\nu/(1+\nu)/(1-2\nu)$ and $G = 0.5E/(1+\nu)$, respectively, in which E is Young's modulus, and ν is the Poisson's ratio.

After processing the Laplace transform, the displacement potential function can be transformed as Miklowitz (1978):

$$\overline{u}_d(r,s) = \frac{f(s)K_1(sr/c_p)}{(2G/r_b)K_1(sr_b/c_p) + (\lambda + 2G)(s/c_p)K_0(sr_b/c_p)} \tag{13}$$

where the superscript bar represents Laplace transform, s is the transformation parameter, K_0 and K_1 are the modified Bessel functions of the second kind of 0th order and 1st order, respectively. $f(s)$ is the transformed solution of $F(t)$ and has the form of

$$f(s) = \frac{T_\sigma P_{CJ}(t_d e^{-t_r s} - t_r e^{-t_d s} - t_d + t_r)}{t_r(t_d - t_r)s^2} \tag{14}$$

Thus, the transformed radial stress and tangential stress can be expressed as Miklowitz (1978):

$$\overline{\sigma}_{dr}(r,s) = f(s)\frac{(2G/r)K_1(sr/c_p) + (\lambda + 2G)(s/c_p)K_0(sr/c_p)}{(2G/r_b)K_1(sr_b/c_p) + (\lambda + 2G)(s/c_p)K_0(sr_b/c_p)} \tag{15a}$$

$$\overline{\sigma}_{d\theta}(r,s) = f(s)\frac{(2G/r)K_1(sr/c_p) - \lambda(s/c_p)K_0(sr/c_p)}{(2G/r_b)K_1(sr_b/c_p) + (\lambda + 2G)(s/c_p)K_0(sr_b/c_p)} \tag{15b}$$

To recover the actual radial and tangential stresses, the above transforms are numerically inverted using the Stehfest algorithm (Jacquot et al. 1983). Using the physical and mechanical parameters given in Sect. 3 and with a borehole radius of 3.225 mm, the time-history curves of explosion stress at $r=25$ mm and the attenuation curves of maximum tensile stresses in the excavation rock and reserved rock for decoupling ratio of 3.5, 4.0, 4.5, 5.0, 5.5 and 5.86 are plotted in Fig. 3. A positive value of stress means rock under tension. In contrast, a negative value of stress represents a rock under compression.

It can be seen from Fig. 3a, b that both the compressive and tensile stresses decrease with the increase of the decoupling ratio, indicating that a higher K_d in air–water coupling blasting leads to smaller damage to the rock. Meanwhile, the peak values of explosion stresses, including peak compressive stress and peak tensile stress in the excavation rock, are much higher than those in the reserved rock, implying more fractures and damage in the excavation rock are formed. Besides, as shown in Fig. 3c, d, the maximum tangential tensile stress quickly attenuates to a low level as it propagates in rock mass, while the maximum radial tensile stress rises first and then reduces with the distance away from the borehole increase. At any distance from the borehole, the difference of maximum tensile stresses, including the maximum radial tensile stress and maximum tangential tensile stress, between excavation rock and reserved rock increases with the increase of K_d, which induces a more asymmetric fracture pattern, i.e. the extent of rock fracture in the excavation rock is much larger than that in the remained rock. Under this scenario, the fracture control is achieved under air–water

coupling blasting and a large decoupling ratio, i.e. a small charge diameter, is conducive to the performance of fracture control.

It should be pointed out that the above results are obtained based on the assumptions of linear-elastic materials and plane strain, and thus the material mixing in the vicinity of the explosive-air–water interface and the non-linear dynamic responses of rock is not considered. Besides, the planer model causes all the energy to go into P-waves, which causes larger compressive and tensile stresses in rock because a relatively large amount of explosion energy goes into S-waves in actual blasting. Hence, some errors inevitably incur. In the following sections, 3D numerical modelling, taking the non-linear responses of explosive, air, water and rock under air–water coupling blasting into account, is presented.

3 Material models and numerical calibration

In this study, the Finite Element method with LS-DYNA code is adopted to model rock blasting since the constitutive models in LS-DYNA library can be used to accurately calculate the pressure generated by explosive detonation and simulate the damage behavior of rock, which is crucial for the current study. Before numerical investigation on air–water coupling blasting, numerical verification is performed against the crack pattern and pressure distribution in experiments of air-coupling blasting and water-coupling blasting conducted by Banadaki (2010). In the blasting experiments, a cylindrical granitic sample (intact Laurentian granite) with 144 mm in out diameter (OD) and 150 mm in height was prepared, and a central borehole with a diameter of 6.45 mm was drilled along the sample axis. A copper tube with a wall thickness of 0.6 mm was tightly installed in the borehole to prevent explosion gas penetration into the cracks caused by explosion shock/stress waves, and thus explosion only generates a fracture network within samples without fragmenting rock samples. Air and water were two coupling mediums used to fill the gap between the inner wall of the copper tube and the outer surface of the peeled Anoline. The peeled Anoline has a core load of 1.2 g/m PETN with an out diameter (OD) of 1.1 mm, and a 0.7-mm-thickness polyethylene sheath covers the strand of PETN. After shots, samples were sliced perpendicular to the sample axis at 25, 75 and 125 mm from the top surface of the sample into four slices. Then, three specified cut surfaces (the top surface of the second slice and the top and bottom surfaces of the third slice. They are named Top cut surface, Middle cut surface and Bottom cut surface, respectively), as shown in Fig. 4a, were polished and dye impregnated to map the fracture patterns with digital photography under high-intensity ultraviolet light.

A 3D model that includes explosive, polyethylene sheath, air, water, copper, and granite with the same dimension as the test sample is built to reproduce the explosion pressure and rock fractures in blasting experiments, as shown in Fig. 4b. In this model, the hexahedral element is used, and non-uniformed mesh is applied to ensure approximate element size. The average element size for rock is 1 mm × 1 mm × 1 mm. To solve the problem of large deformation during rock blasting, the *Arbitrary-Lagrange-Euler* method (*ALE_MULTI-MATERIAL_GROUP) is applied for explosive, polyethylene, air and water materials, while the *Lagrangian* formulation is used for copper and rock materials. The material models and state equations (EOSs) for rock, explosive, polyethylene, air, water and copper are summarized as follows.

3.1 Material models and equation-of-states

3.1.1 Rock

The material type of Mat_Riedel_Hiermaier_Thoma (RHT model), whose strength criteria are expressed in terms of three stress limit surfaces, i.e., the initial elastic yield surface, the failure surface and the residual friction surface, is chosen for simulating the blast-induced rock fracturing (Borrvall and Riedel 2011; Riedel et al. 1999). In the RHT model, pressure is expressed using the Mie-Gruneisen form with a polynomial Hugoniot curve and a $P - \alpha$ compaction Equation-of-state (EOS) considering the porous property of brittle material. Meanwhile, this model considers the effects of confining pressure, high strain rate, strain hardening and damage softening. Hence, it is appropriate to model the dynamic behavior of rock under blast loading. In the RHT model, 38 parameters are used to model the dynamic response of rock accurately. The basic physical and mechanical parameters, such as Density (2660 kg/m^3), Shear Modulus

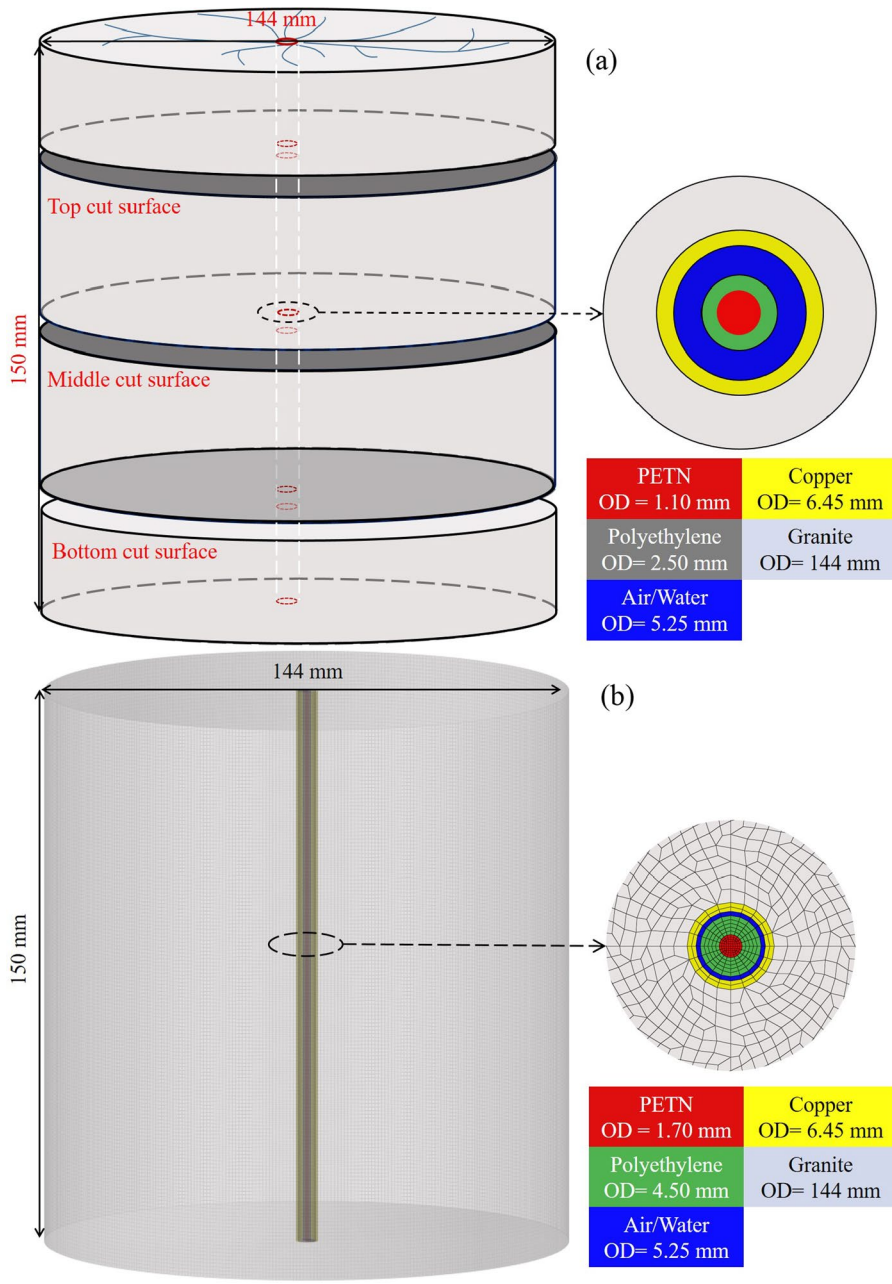

Fig. 4 **a** Granitic sample in blasting test and **b** 3D numerical model and local mesh

(20.28 GPa), Porosity (0.64%), uniaxial compressive strength (259 MPa), uniaxial tensile strength (12.79 MPa), Young's modulus (47.39 GPa), Poisson's ratio (0.17) and P-wave velocity (4390 m/s), are obtained from the test by Banadaki's (2010) and related report by Iqbal (2004). The other parameters are determined by theoretical calculations or from References, as given below:

3.1.1.1 Strain rate parameters The dynamic strength of rock is strain rate dependent, and the strain rate dependence in the RHT model is expressed as LSTC (2015):

$$F_{\mathrm{r}}(\dot{\varepsilon}_p) = \begin{cases} (\dot{\varepsilon}_p / \dot{\varepsilon}_0^t)^{\beta_t} & (P \le -f_t/3) \\ \frac{P+f_t/3}{f_c/3+f_t/3}(\dot{\varepsilon}_p / \dot{\varepsilon}_0^c)^{\beta_c} - \frac{P-f_c/3}{f_c/3+f_t/3}(\dot{\varepsilon}_p / \dot{\varepsilon}_0^c)^{\beta_t} & (-f_t/3 < P < f_t/3) \\ (\dot{\varepsilon}_p / \dot{\varepsilon}_0^c)^{\beta_c} & (P \ge f_c/3) \end{cases} \tag{16}$$

where $F_r(\dot{\varepsilon_p})$ is the strain strength factor, $\dot{\varepsilon_p}$ is the strain rate, P is the pressure.$\dot{\varepsilon_0^c}$ and $\dot{\varepsilon_0^t}$ are the reference strain rate under compression and tension, respectively. f_c and f_t are the uniaxial compressive strength and tensile strength, respectively. β_c and β_t are the material constants for compression and tension, respectively. Based on the dynamic compressive and tensile strengths of rock under different strain rates summarized by Zhang and Zhao (2014), the relationship between the strain rate and rock compressive or tensile strengths was obtained by Xie et al. (2017) through curve fitting, and it is presented in Eq. (17a) under compression and given in (17b) under tension. So, β_c and β_t are 0.026 and 0.007, respectively. Meanwhile, $\dot{\varepsilon_0^c} = 3.0\times10^{-5}$ s^{-1}, $\dot{\varepsilon_0^t} = 3.0\times10^{-6}$ s^{-1}.

$$F_r^c(\dot{\varepsilon}_p) = \begin{cases} (\dot{\varepsilon}_p / \dot{\varepsilon}_0^c)^{0.026} & (\dot{\varepsilon}_p \le 30\ \mathrm{s}^{-1}) \\ 0.512\,\dot{\varepsilon}_p^{1/3} & (\dot{\varepsilon}_p > 30\ \mathrm{s}^{-1}) \end{cases} \tag{17a}$$

$$F_r^t(\dot{\varepsilon}_p) = \begin{cases} (\dot{\varepsilon}_p / \dot{\varepsilon}_0^c)^{0.007} & (\dot{\varepsilon}_p \le 10^{-1}\ \mathrm{s}^{-1}) \\ 2.4\,\dot{\varepsilon}_p^{1/3} & (\dot{\varepsilon}_p > 10^{-1}\ \mathrm{s}^{-1}) \end{cases} \tag{17b}$$

3.1.1.2 Failure surface parameters The failure surface parameters A and N can be determined by Borrvall and Riedel (2011):

$$\sigma_f^*(P^*, F_r) = A(P^* - F_r/3 + (A/F_r)^{-1/N})^N (3P^* \ge F_r) \tag{18}$$

where P^* is the normalized pressure, $P^* = P/f_c$, where $P = 1/3(\sigma_1+\sigma_2+\sigma_3)$; $\sigma_f^*(F_r)$ is the normalized strength, $\sigma_f^* = \sigma_f / f_c$, where $\sigma_f = \sqrt{\frac{1}{2}\left[(\sigma_1-\sigma_2)^2 + (\sigma_2-\sigma_3)^2 + (\sigma_3-\sigma_1)^2\right]}$. When rock is in a quasi-static state, i.e. $\dot{\varepsilon_p} = 3.0\times10^{-5}$ s^{-1} and $F_r = 1$, A and N can be calculated by taking the triaxial compressive strengths of rock under various confining pressures obtained by the Hoek–Brown criterion into Eq. (18). For intact rock, the Hoek–Brown criterion is defined by Hoek and Brown (1980):

$$\sigma_1 = \sigma_3 + f_c(m_i\frac{\sigma_3}{f_c} + s)^{1/2} \tag{19}$$

where σ_1 and σ_3 are maximum and minimum effective stresses at failure, s and mi are intact rock constants. According to Banadaki (2010), Eq. (19) can be written as:

$$\sigma_1 = \sigma_3 + 259_c\left(29\frac{\sigma_3}{259} + 1\right)^{1/2} \tag{20}$$

and the mechanical parameters of rock under various confining pressures can be calculated and listed in Table 1. Taking the P^* and σ_f^* values under confining stresses of 10 and 100 MPa into Eq. (18), $A = 2.57$ and $N = 0.75$ are obtained.

Under blast loading, the maximum reduction in rock strength is given as a function of relative pressure:

$$Q(P^*) = Q_0 + BP^* \tag{21}$$

where Q_0 is the ratio between the radii of the tensile and compressive meridians, and B is the lode angle dependence factor. Equation (21) can be written as $Q(P^*) = 0.68 + 0.05P^*$ based on the curve regression results reported by Yu (1998). Therefore, $Q_0 = 0.68$ and $B = 0.05$.

3.1.1.3 Damage parameters The damage level D of the RHT model is expressed by:

$$D = \sum\left(\Delta\varepsilon_p/\varepsilon_f\right) \tag{22}$$

where $\Delta\varepsilon_p$ is the accumulated plastic strain, ε_f is the failure strain under pressure P expressed as:

$$\varepsilon_f = D_1 - (P^* - (1-D)P_t^*)^{D2} \tag{23}$$

where P_t^* is the failure cut-off pressure, D_1 and D_2 are damage constants. In the current numerical modelling, the parameters of $D_1 = 0.04$ and $D_2 = 1.0$ are

Table 1 Mechanical parameters of rock under various lateral pressures

$\sigma_2=\sigma_3$/MPa	σ_1/MPa	P/MPa	σ_f/MPa	P^*	σ_f^*
0.00	− 12.79	− 4.26	12.79	− 0.02	0.05
0.00	259.00	86.33	259.00	0.33	1.00
10.00	387.08	135.69	377.08	0.52	1.46
50.00	715.31	271.77	665.31	1.05	2.57
100.00	1004.53	401.51	904.53	1.55	3.49
200.00	1452.71	617.57	1252.71	2.38	4.84

determined from Reference Brannon and Leelavanichkul (2009).

3.1.1.4 EOS parameters In the RHT model, the EOS is described as follows:

$$P_{EOS} = \frac{1}{\alpha}((B_0 + B_1\mu)\alpha_0\rho_r e + A_1\mu + A_2\mu^2 + A_3\mu^3) \quad \mu > 0 \tag{24}$$

where B_0 and B_1 are material constants; α_0 is the initial porosity, ρ_r is the initial density of rock, e is the internal energy per unit mass, μ is the volumetric strain, A_1, A_2 and A_3 are the Hugoniot polynomial coefficients which can be calculated by the derived formulation of Xie et al. (2017) as follows:

$$A_1 = \alpha_0\rho_r c^2 \tag{25a}$$

$$A_2 = \alpha_0\rho_r c^2(2k - 1) \tag{25b}$$

$$A_3 = \alpha_0\rho_r c^2[(3k - 1)(k - 1)] \tag{25c}$$

where c is the wave velocity, and k is the material constant for granite which is 1.084 (Pan et al. 2022). Hence, A_1, A_2 and A_3 can be calculated as 51.57, 60.23 and 9.76 GPa, respectively. Moreover, the elastic limit pressure, i.e. the pore crush pressure, is taken as 2/3 of the uniaxial compressive strength according to Riedel et al. (2009), which is 172.67 MPa. In addition, the remaining parameters are obtained from References Borrvall and Riedel (2011), Xie et al. (2017), and the parameters used in RHT model for rock are listed in Table 2.

3.1.2 Explosive

In LS-DYNA, the material type of Mat_High_Explosive_Burn together with EOS of Jones–Wilkins–Lee (JWL) is widely used to simulate the pressure generated by the expansion of detonation products (Liu et al. 2018, 2019b; Wei et al. 2009). This JWL EOS defines the detonation pressure P_e in the form of Lee et al. (1968):

Table 2 Parameters for rock

Parameter	Value	Parameter	Value
Mass density ρ_r (kg/m^3)	2660	Compressive strain rate dependence exponent β_c	0.026
Elastic shear modulus *SHEAR* (GPa)	20.28	Tensile strain rate dependence exponent β_t	0.007
Eroding plastic strain *EPSF*	2.0	Volumetric plastic strain fraction in tension *PTF*	0.001
Parameter for polynomial EOS B_0	1.22	Compressive yield surface parameter *GC**	0.53
Parameter for polynomial EOS B_1	1.22	Tensile yield surface parameter *GT**	0.70
Parameter for polynomial EOS T_1 (GPa)	51.57	Shear modulus reduction factor *XI*	0.50
Parameter for polynomial EOS T_2 (GPa)	0.0	Damage parameter D_1	0.04
Failure surface parameter *A*	2.57	Damage parameter D_2	1.00
Failure surface parameter *N*	0.75	Minimum damaged residual strain *EPM*	0.015
Compressive strength f_c (MPa)	259	Residual surface parameter *AF*	1.60
Crush pressure *PEL* (MPa)	172.67	Residual surface parameter *NF*	0.61
Relative shear strength *FS**	0.21	Gruneisen gamma *GAMMA*	0.0
Relative tensile strength *FT**	0.10	Hugoniot polynomial coefficient A_1 (GPa)	51.57
Lode angle dependence factor Q_0	0.68	Hugoniot polynomial coefficient A_2 (GPa)	60.23
Lode angle dependence factor *B*	0.05	Hugoniot polynomial coefficient A_3(GPa)	9.76
Reference compressive strain rate *EOC* (S^{-1})	3.0E−5	Compaction pressure *PCO* (GPa)	6.0
Reference tensile strain rate ETC (S^{-1})	3.0E−6	Porosity exponent *NP*	3.0
Break compressive strain rate *EC* (S^{-1})	3.0E+25	Initial porosity α_0	1.006
Break tensile strain rate *ET* (S^{-1})	3.0E+25		

Table 3 Parameters for explosive (Banadaki 2010)

ρ_e (kg/m^3)	*VOD* (m/s)	E_{e0} (GPa)	P_{CJ} (GPa)	A_e (GPa)	B_e (GPa)	R_1	R_2	ω
1260	6470	7.03	14.3	5.66×10^2	20.4	5.98	1.81	0.28

Table 4 Parameters for polyethylene (Li et al. 2021a, b, c)

ρ_{p0} (kg/m^3)	C_p (m/s)	V_{p0}	S_1	S_2	S_3	γ_p	α_p
915	2901	1.0	1.481	0	0	1.64	0

Table 5 Parameters for air

ρ_{a0} (kg/m^3)	E_{a0} (J/m^3)	γ_a	C_0	C_1	C_2	C_3	C_4	C_5	C_6
1.29	2.5×10^5	1.4	0	0	0	0	0.4	0.4	0

$$P_e = A_e\left(1-\frac{\omega}{R_1V_e}\right)e^{-R_1V_e} + B_e\left(1-\frac{\omega}{R_2V_e}\right)e^{-R_2V_e} + \frac{\omega E_e}{V_e} \tag{26}$$

where V_e is the relative volume of the detonation product, E_e is the detonation energy per unit volume with an initial value of E_{e0}, and A_e, B_e, R_1, R_2 and ω are explosive constants. Generally, the parameters for explosive are determined based on the specifications of explosive. In the current modelling, the parameters for explosives used in blasting tests are obtained in Banadaki tests and listed in Table 3.

3.1.3 Polyethylene

To simulate the behavior of polyethylene sheath that covers the strand of PETN, the combination of Mat_Null and Gruneisen EOS in the LS-DYNA library is adopted. The Gruneisen EOS with cubic shock velocity–particle velocity (v_s–v_p) defines pressure for compressed polyethylene as LSTC (2015):

$$P_p = \frac{\rho_p C_p^2\mu_p\left[1+\left(1-\frac{\gamma_{p0}}{2}\right)\mu_p-\frac{\alpha_p}{2}\mu_p^2\right]}{\left[1-(S_1-1)\mu_p-S_2\frac{\mu_p^2}{\mu_p+1}-S_3\frac{\mu_p^3}{(\mu_p+1)^2}\right]^2}+(\gamma_{p0}+\alpha_p\mu_p)E_p \tag{27}$$

where P_p is the pressure of polyethylene, γ_{p0} is the Gruneisen gamma, α_p is the first order volume correction to γ_p, and μ_p is equal to $\rho_p/\rho_{p0}-1$ with ρ_p and ρ_{p0} being the current and initial density of polyethylene, respectively; C_p is the intercept of v_s-v_p curve, E_p is the internal energy per unit volume with an initial value of E_{p0}, and S_1, S_2 and S_3 are the coefficients of the slope of the v_s-v_p curve, respectively. The parameters for polyethylene are listed in Table 4.

3.1.4 Air

Air is modelled by the material type Mat_Null with a specific Linear_Polynomial EOS, and this EOS is expressed as LSTC (2015):

$$P_a = C_0 + C_1\mu_a + C_2\mu_2 + C_3\mu_3 + (C_4 + C_5 + C_6\mu_a^2)E_a \tag{28}$$

where P_a is the pressure of air, E_a is the internal energy per volume, μ_a defines the compression of air by $\mu_a=(\rho_a/\rho_{a0})-1$ with ρ_a and ρ_{a0} being the current and initial density of air, respectively. C_0, C_1, C_2, C_3, C_4, C_5 and C_6 are material constants of air, and C_4 and C_5 can be calculated by $C_4=C_5=\gamma_a-1$ with γ_a being the ratio of specific heats of air. The parameters for air are well documented with previous experimental calibrations and listed in Table 5.

3.1.5 Water

Water is modeled by the material type of Mat_Null combined with the Gruneisen EOS (Eq. 27), and this combination is widely used for simulating water-filled blasting and underwater explosion (Zhang et al. 2012, 2014). The parameters for water are also well documented with previous experimental calibrations and listed in Table 6.

Table 6 Parameters for water

ρ_{w0} (kg/m^3)	C_w (m/s)	E_{w0} (J/m^3)	S_{w1}	S_{w2}	S_{w3}	γ_w	α_w	V_{w0}
1000	1480	1.89×10^6	2.56	− 1.986	1.2268	0.35	0	1.0

Table 7 Parameters for copper (Li et al. 2021a, b, c)

Parameter	Value	Parameter	Value
Mass density (kg/m^3)	8330	Material constant C	0.025
Young's modulus (GPa)	138	Material constant n	0.31
Poisson's ratio	0.35	Material constant m	1.09
Melt temperature (K)	1357.8	EOS constant C_c	3940
Initial internal energy E_{c0} (J/m^3)	0	EOS constant α_c	0.47
Initial relative volume V_{c0}	1.0	EOS constant S_{c1}	1.49
Gruneisen gamma γ_c	2.0	EOS constant S_{c2}	0
Material constant A_c (GPa)	8.963×10^{-2}	EOS constant S_{c3}	0
Material constant B_c (GPa)	2.916×10^{-1}		

3.1.6 Copper

Material type of Mat_Johnson_Cook together with Gruneisen EOS (Eq. 27) is chosen to model the copper behavior under blast loading, and the flow stress in this material model is expressed as LSTC (2015):

$$\sigma = \left(A_c + B_c\bar{\varepsilon}^{p^n}\right)\left(1 + C_c \ln \dot{\varepsilon}^*\right)(1 - T^{*m}) \tag{29}$$

where A_c, B_c, C, n and m are constants of copper. The parameters for copper are listed in Table 7.

3.2 Numerical calibration

3.2.1 Numerical modelling of air and water coupling blasting

With the above material models and EOSs, the initiation and propagation of fractures induced by air-coupling blasting and water-coupling blasting in experiments are reproduced in LS-DYNA, and the fracture evolution at 16, 28 and 150 us is demonstrated in Fig. 5. The consecutive processes of rock fracturing induced by air and water coupling blasts can be briefly described as follows:

- After the strand of PETN is detonated from the top surface of the sample, a conical crushed zone is immediately created around the borehole due to explosion shock waves. ($t<6$ us)
- Then, blast-induced rock fracture extends to the sample bottom, and spalling damage appears and radially develops at the bottom surface of the sample since the downwards propagated stress waves reflect and return to the sample, changing into tensile stress waves. Simultaneously, radial cracks develop from the edge of the crushed zone due to the tangential tensile stress component of explosion stress waves exceeding the dynamic tensile strength of the rock. ($t<28$ us)
- Next, radial cracks continuously develop until they reach the cylindrical surface, and circumferential spalling cracks generate near the cylindrical surface because radial compressive stress waves reflect at this cylindrical surface and change into tensile stress waves, which are still higher than the dynamic tensile strength of rock. ($t<150$ us, this stage only appears in water-coupling blasting)
- At last, the propagation of blast-induced fractures arrests, and a 3D final fracture network is produced ($t=150$ us). The fracture network becomes denser from the top to bottom surface because the stress field gets stronger as the strand of PETN explosion progresses from the top towards the bottom of the sample due to the superposition of blast-induced stress waves and reflected stress waves.

It can be observed in Fig. 5 that the extent of rock fracturing under air-coupling blasting is much smaller than that under water-coupling. In

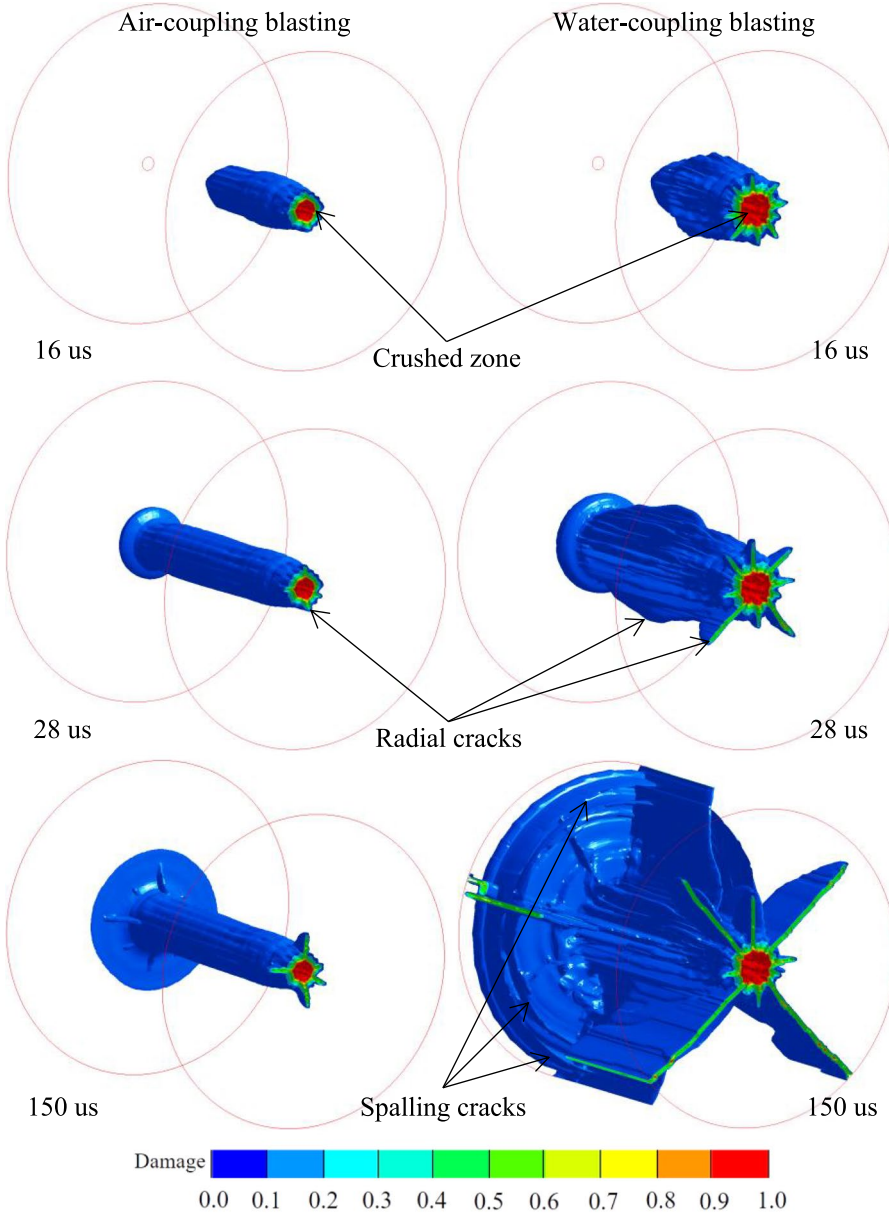

Fig. 5 Fracture evolution in rock blasts using air and water coupling

air-coupling blasting, blast-induced radial cracks develop at a very short distance away from the borehole, and the spalling damage with a small thickness is created at the bottom surface near the borehole. In comparison, long radial cracks induced by water-coupling blasting cross through rock samples. Meanwhile, spalling cracks close to the cylindrical surface and much more extensive spalling damage at the bottom surface are generated after the detonation of the water-filled borehole.

3.2.2 Comparison of tested and simulated results

The tested fracture networks in specified cut surfaces are shown in Fig. 6a. In water-coupling blasting, both the length and number of blast-induced cracks increase by moving from top to bottom of the rock sample due to the intensified stress field at the sample bottom. Besides, variations in crack patterns also occur maintaining a distance from the borehole change in the radial direction. Short cracks

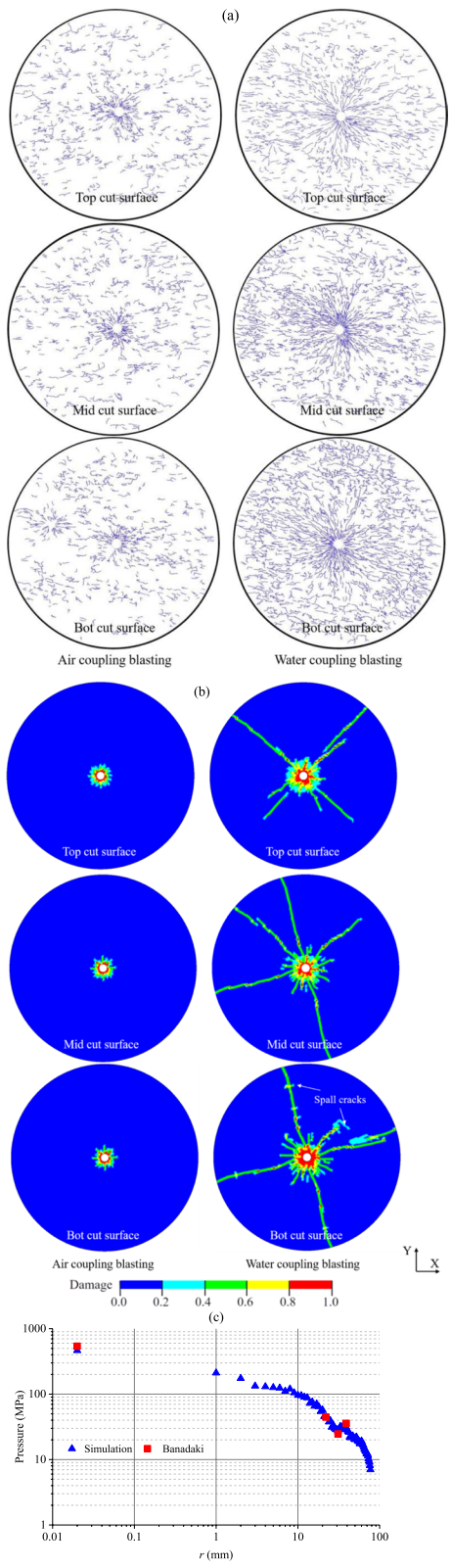

Fig. 6 Comparison of **a** tested and **b** simulated crack patterns in three specified cut surfaces under air-coupling blasting and water-coupling blasting, and **c** comparison of tested and simulated explosion pressure under water-coupling blasting at a level of 80 mm from the top surface

in all three cut surfaces are densely populated close to the borehole, whereas few long cracks propagate towards the outer boundary. By contrast, the phenomenons that the length and density of cracks change in the axial and radial directions of the sample are not obvious in air-coupling blasting. With air-coupling, only some short cracks grow in the vicinity of the borehole in all cut surfaces as less explosion energy is transmitted into rock.

The crack patterns in three specified cut surfaces obtained in numerical modelling are presented in Fig. 6b. In general, the rock crack is the degeneration and discontinuity which can be reflected by the damaged elements in LS-DYNA. Using the RHT model, the damage of rock material (D) accumulates from 0 to 1, and the extent of rock damage can be denoted with different D values from slight degradation to fully damaged. By comparing the crack patterns in photographs taken from the tested sample and in cut surfaces of the calculated numerical model, it is evident that the number and length of main cracks, and the crack distribution in the numerical simulation are in good agreement with those in the physical experiment, and a damage level of 0.2 can be considered as the threshold for crack formation. Note that the tested crack patterns show more discontinuous flaws. This is because many pre-existing microcracks that develop to be small discontinuous and short cracks under blast loading initially exist in the physical samples, and these microcracks are not possible to be constructed and calculated in LS-DYNA owing to the limitation of the element size. In addition, the simulated explosion pressure distribution in simulation agrees well with that in the blasting test, as presented in Fig. 6c. Hence, it can be concluded that the pressure variation and fracture network induced by air and water coupling blasts are reasonably predicted using the current developed numerical model. In the subsequent simulation, the currently developed numerical model is used to simulate air–water coupling blasting.

4 Numerical modelling of air–water coupling blasting

4.1 Computational model

To simulate the air–water coupling blasting, a 3D model with the same dimension as the laboratory rock sample is built, as shown in Fig. 7. The gap between the 1.1-mm-diameter central charge and borehole wall is simultaneously filled with air on the reserved rock side and water on the excavated rock side with an air–water ratio of 1:1 (the decoupling ratio is 5.86). The plastic bag or thin PVC pipe is overlooked in model construction due to its low strength and small thickness. The excavated and reserved rocks are divided by the designed excavation line (denoted by a red dash line). In this model, hexahedral elements are also used, and the element size for rock is still 1 mm × 1 mm × 1 mm. The elements at the interfaces between the explosive, air, water and rock parts share common nodes.

In the simulation of air–water coupling blasting, an explosive is ignited at the model top. During the calculation, the blasting stresses on the water side transfer faster than on the air side because the wave velocity in water is higher than in air. Consequently, the water inevitably squeezes into the air side, and obviously, air–water coupling blasting is a mixing problem between water and air. In the current simulation, this mixing problem of multi-materials is solved by the Multi-material ALE algorithm method. Using this method, explosive materials, air and water are allowed to mix in each element in Parts of explosive, air and water during calculation. Additionally, the pressure curves at 6 target points listed in Table 8 are recorded to analyse the pressure change under air–water coupling blasting.

4.2 Blasting process and analysis

Based on the calibrated material models and EOSs, the explosion pressure evolution and fracture network

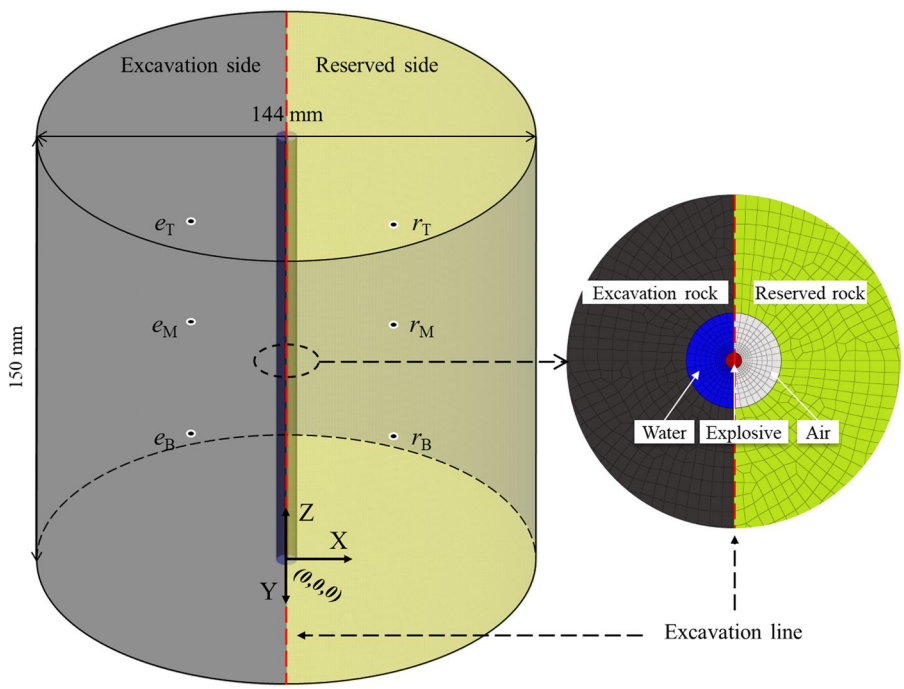

Fig. 7 Computational model for air–water coupling blasting

Table 8 Locations of target points

No	r_T	e_T	r_M	e_M	r_B	e_B
Coordinate (mm)	(25,0,125)	(− 25,0,125)	(25,0,75)	(− 25,0,75)	(25,0,25)	(− 25,0,25)

development under air–water coupling blasting at 16, 28 and 150 us after detonation are shown in Fig. 8.

Once the explosive is initiated at the model top, explosion shock/stress waves immediately transmit through coupling medium and travel in rock, generating a cone-shape explosion stress wavefront, as shown in Fig. 8a. Simultaneously, a cone-shaped high-pressure zone behind this stress wavefront is formed due to the superimposition of explosion shock/stress waves in the direction of borehole axil. Note that the extent of a high-pressure zone on the water-coupling side is bigger than that on the air-coupling side. Water performs well in stress transmission due to its incompressibility and large wave impedance. Moreover, high explosion pressure transfers into excavation rock. Conversely, air acts as a buffer layer between explosive and rock and reduces the amplitude of explosion stress waves because of its characteristics of high compressibility and low wave impedance, which agrees well with the theoretical results as depicted in Figs. 2 and 3. At $t = 16$ us, a crushed zone in the shape of a cone is created, as shown in Fig. 8d, and the crushed zone in excavation rock is more significant than that in reserved rock since the explosion shock/stress waves transmit in the rock through the water with higher magnitude compared with those passing air.

Then, with the explosive burning toward to model bottom, the explosion stress wavefront moves downward and away from the borehole. When the explosion stress wavefront reaches the cylindrical surface, the compressive stress waves reflect into rock and change into tensile stress waves, as shown in Fig. 8b. In this stage, explosion stresses, including compressive stress and tensile stress, get stronger with the increasing distance from the model top due to the reflection and superposition of explosion stress waves. It is worth noting that more reflected tensile stress waves are generated in rock on the water-coupling side, which appears to be very effective in initiating and propagating spalling cracks in excavation rock. At $t = 28$ us, blast-induced fractures extend to the bottom surface, as shown in Fig. 8e. At this time, the expansion of the crushed zone stops, and radial fractures continue to propagate. Two prominent radial cracks grow along the designed excavation line and thus separate the excavation rock from the remaining rock, generating a smooth excavation boundary. Meanwhile, spalling damage at the bottom surface on the water-coupling side is produced because of the reflection of explosion stress waves. At $t = 150$ us, blast-induced tensile stress waves decay below the dynamic tensile strength of rock, and low explosion pressure remains in the vicinity of the borehole because residual explosion products apply loads on the inner boundary of the crushed zone, as shown in Fig. 8c. Consequently, crack propagation arrests, and the final 3D fracture network is generated as shown in Fig. 8f.

It can be observed in Fig. 8 that a bigger fractured zone is created in the excavation rock. The crack volume, i.e. the volume of damaged elements whose damage level exceeds 0.2, in the excavation zone is 2.1×10^{-5} m^3, and it is much bigger than that in the reserved rock (1.3×10^{-5} m^3), indicating that the rock in the excavation zone is effectively fragmented while the surrounding rock is reasonably protected. Herein, the cracking volume does not refer to the breakage volume of rock, but it adequately reflects the fracturing extent, indicating that the fracture development is well controlled in fracture control blasting using air–water coupling.

The time-history curves of explosion pressure at target points are shown in Fig. 9. Evidently, the peak pressures in compression and tension on water-coupling side are much higher than those on air-coupling side, which is well in agreement with the theoretical results in Fig. 3. Besides, by moving from the model from top to bottom, these peak values increase. This is mainly caused by the superimposition of stress waves from explosive detonation at different heights.

The crack patterns at the model's top and bottom surfaces under air–water coupling blasting are presented in Fig. 10. It can be seen that more and longer cracks in rock on the water-coupling side are produced. As theoretically analyzed before, this is mainly caused by the difference in wave impedance between air and water. This difference in wave impedance further induces discrepancies in stress transmission and stress propagation between excavation rock and reserved rock, consequently leading to anisotropy in rock fracturing. Besides, it is noted that the rock cracking at the bottom surface is intensified, primarily caused by the superposition and reflection

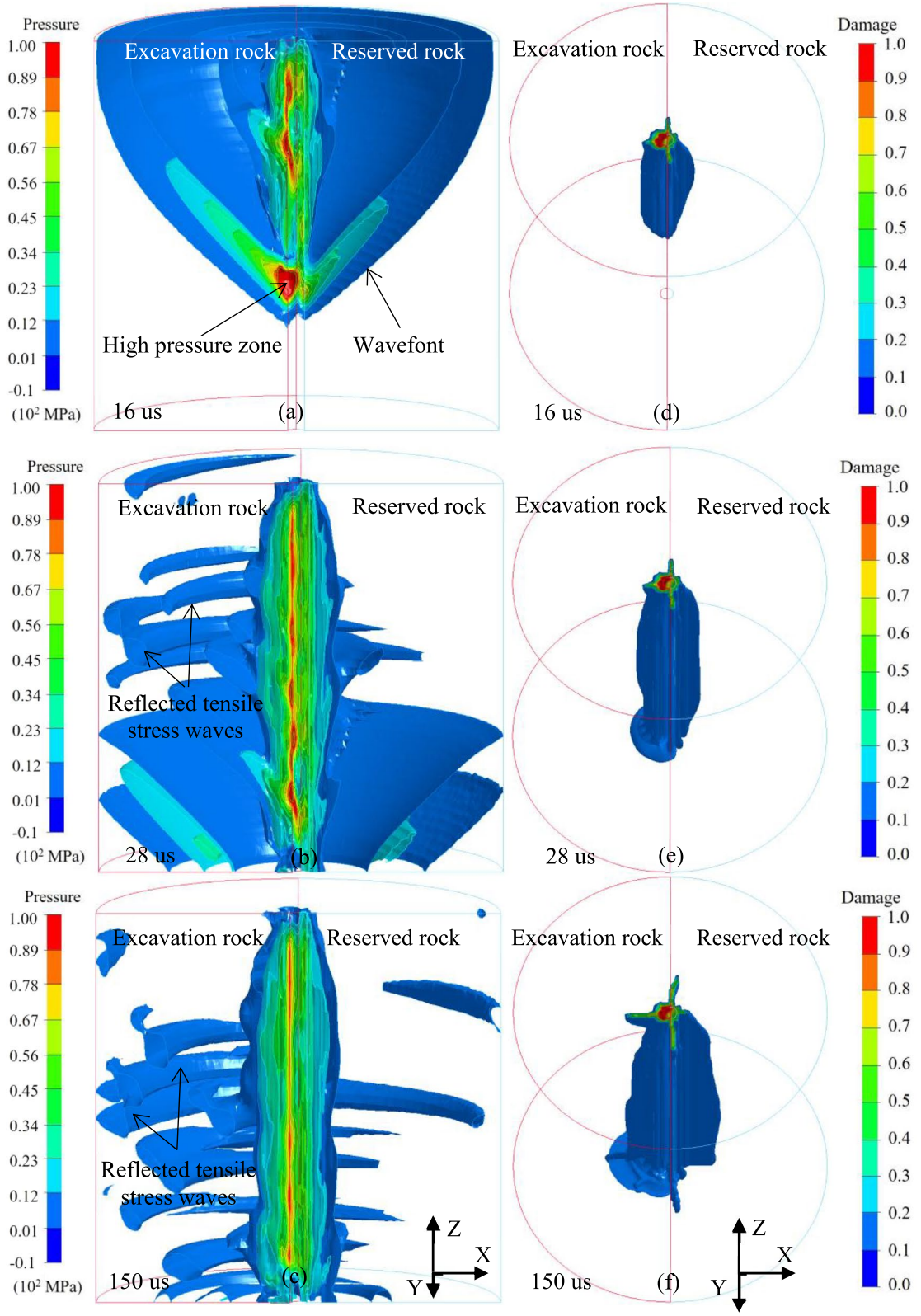
Pressure
1.00
0.89
0.78
0.67
0.56
0.45
0.34
0.23
0.12
0.01
-0.1
(10² MPa)
Excavation rock
Reserved rock
High pressure zone
Wavefont
16 us
(a)
Damage
1.0
0.9
0.8
0.7
0.6
0.5
0.4
0.3
0.2
0.1
0.0
Reflected tensile stress waves
28 us
(b)
(d)
(e)
150 us
(c)
(f)
Z
X
Y

◂**Fig. 8** Explosion pressure and fracture networks induced by air–water coupling blasting at 16, 28 and 150 us

of explosion stress waves. During blasting, more and more extended fractures are created as the distance from the detonation point increases, owing to the explosion stress field getting stronger with the distance away from the initiation point along the borehole axial.

During air–water coupling blasting, explosion energy travels into rock and transfers to internal energy I_E and kinetic energy K_E. Internal energy, including surface fracture energy, internal cracking and damage energy, and strain energy, is mainly consumed in generating new fractures, while kinetic energy primarily plays a role in moving rock fragmentation. Hence, the ratio of internal energy to kinetic energy I_E/K_E can be used to evaluate the energy utilization efficiency of explosive detonation. The greater the I_E/K_E is, the higher the utilization efficiency of blasting energy is. Figure 11a presents curves of kinetic energy. A more considerable peak value of kinetic energy appears in excavation rock, implying more moving fragments generated on the water-coupling side. Figure 11b shows curves of I_E/K_E. It can be seen that the I_E/K_E in excavation rock is higher than that in the remaining rock, which indicates that in air–water coupling blasting, the utilization efficiency of explosion energy in excavation rock is higher. This finding reveals a crucial part of how air–water coupling blasting archives fracture control.

5 Discussions

In air–water coupling blasting, the explosion energy transmitted into rock is significantly affected by air–water ratio K and decoupling ratio K_d, which are important for fracture control. Herein, parametric studies are conducted using numerical modelling to investigate the influences of K and K_d on the performance of fracture control as follows.

5.1 Effects of air–water ratio

To investigate the effects of air–water ratio K on fracture control, with a given 1.1-mm-diameter charge, air–water coupling blasting is simulated with $K=8/2$, 7/3, 6/4, 4/6 and 3/7, and the obtained crack patterns at the top and bottom surfaces of model are presented in Fig. 12. It can be observed that with different K, more and longer blast-induced fractures are generated in the excavation rock compared with those in the remaining rock, and thus directional rock cracking is achieved. In particular, when $K>1$, no crack penetrates the remaining rock at the top surface, whereas some predominant radial cracks propagate in the excavation rock.

With the decrease of K, the crushed zone induced by air–water coupling blasting gradually expands on the water coupling side. Meanwhile, denser and longer radial cracks are formed because more explosion energy travels into the rock, especially in the excavation rock. This suggests that lower K leads to

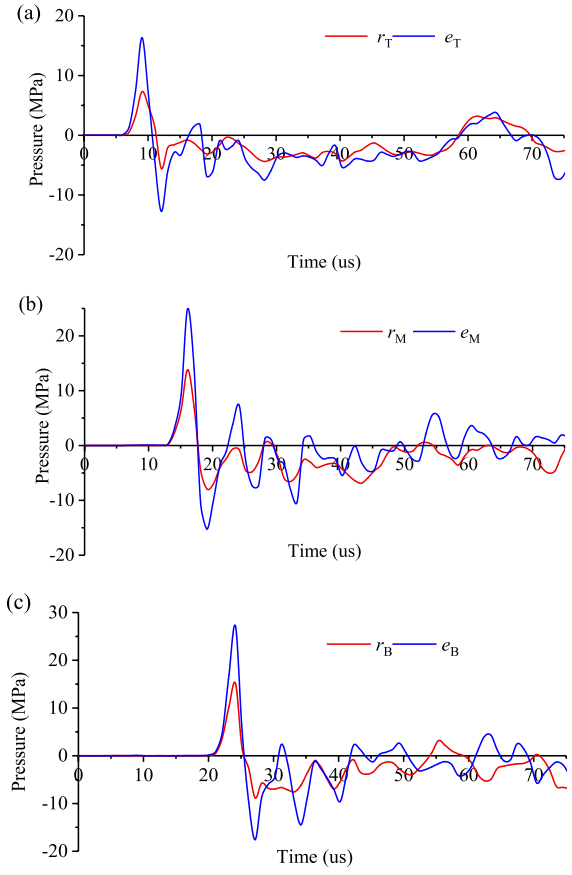

Fig. 9 Time-history curves of explosion pressure at target points: **a** $z=125$ mm, **b** $z=75$ mm, **c** $z=25$ mm

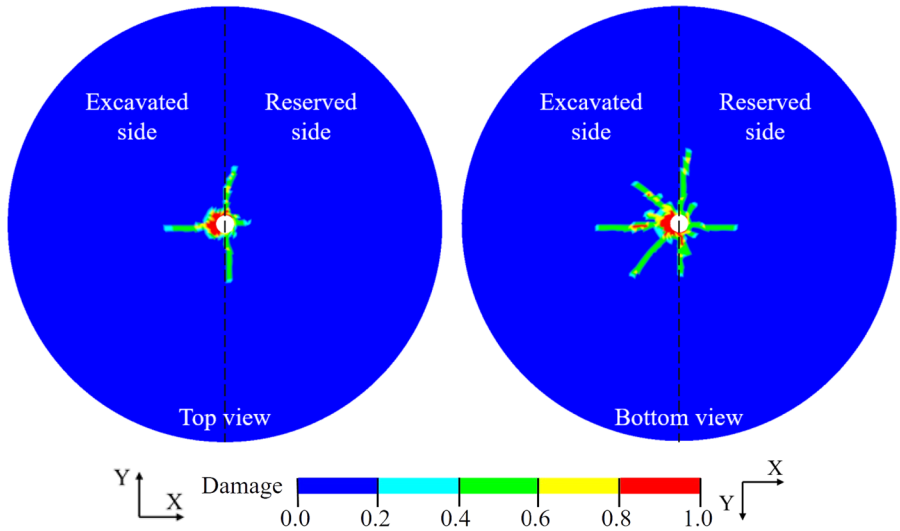

Fig. 10 Crack patterns at top and bottom surfaces

more explosion energy spreading into rock. Therefore, a higher explosion pressure pulse transfers into rock when the water in the borehole increases, producing more and longer fractures. However, as shown in Fig. 12, with the reduction of K, although the blast-induced fractures mostly develop in excavation rock. The rock damage aggravates in the reserved rock too, and thereby the performance of damage control of surrounding rock in air–water coupling blasting worsens.

In air–water coupling blasting, the performance of fracture control can be evaluated by the ratio of crack volume in excavation rock over crack volume in reserved rock (E/R). A larger value of E/R means a better performance of fracture control. Figure 13 presents the variations in crack volume and E/R vs. K. It can be found that the crack volumes on both sides of the excavation boundary reduce as K increases. This can be expected because the increased air in the borehole weakens explosion energy transmission, producing fewer and shorter fractures. Moreover, the curve of E/R rises with increasing K, indicating that more air (less water) in the borehole leads to a bigger discrepancy in fracture propagation between the excavation and reserved rock. Further speaking, the performance of fracture control blasting gets better with the

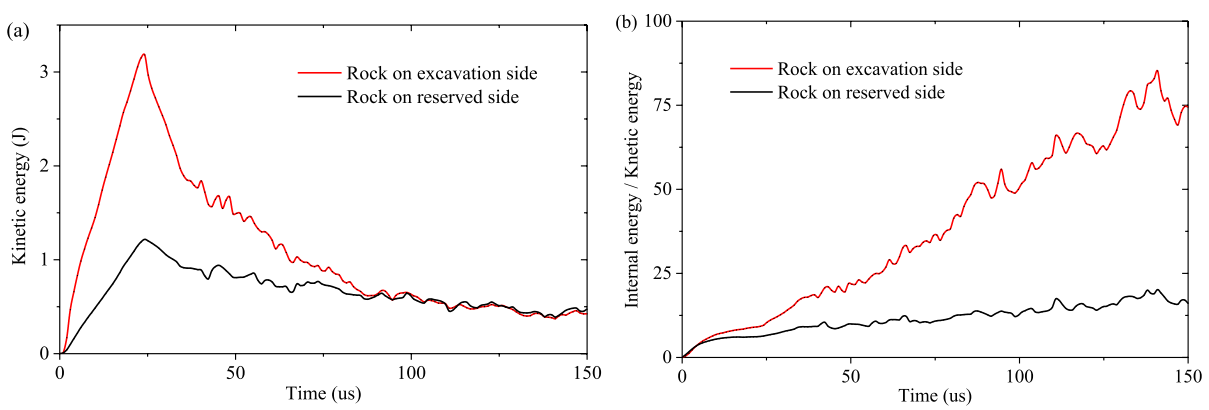

Fig.11 Energy change in the rock under air–water coupling blasting: **a** kinetic energy, **b** the ratio of internal energy over kinetic energy

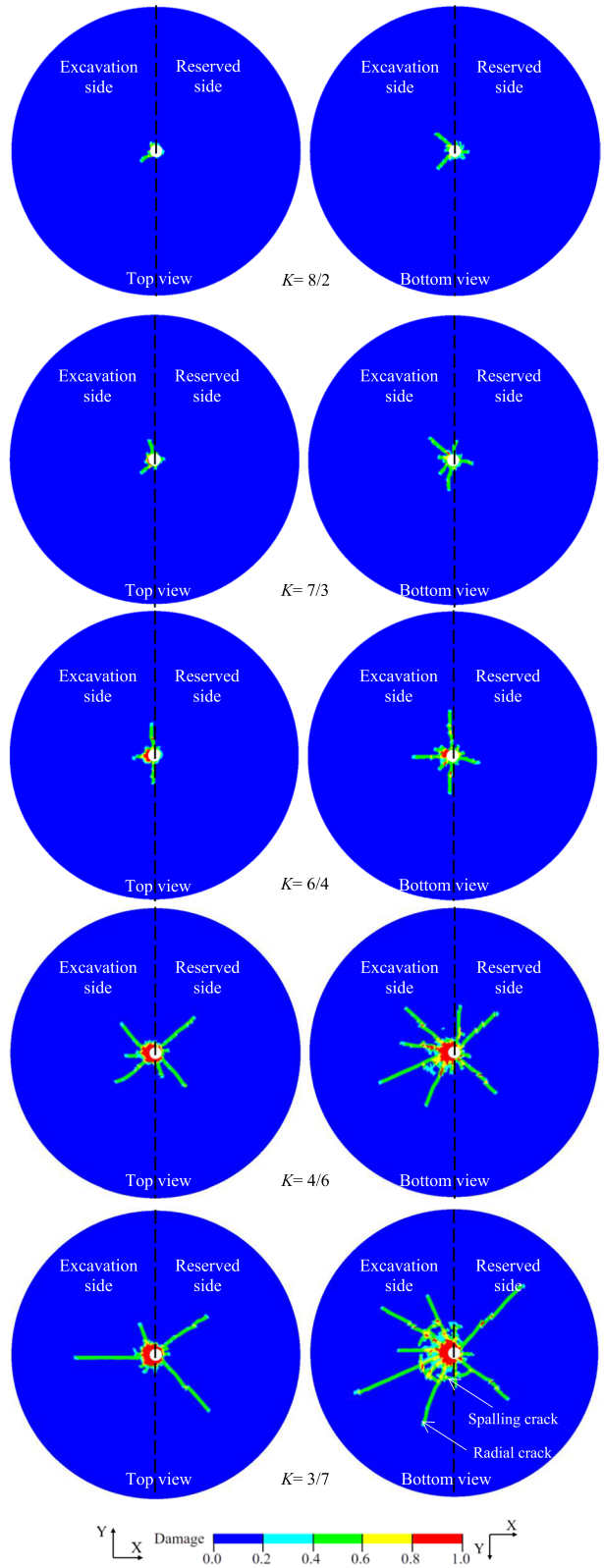

Fig. 12 Crack patterns at the top and bottom surfaces induced by water–air coupling blasting with various *K*

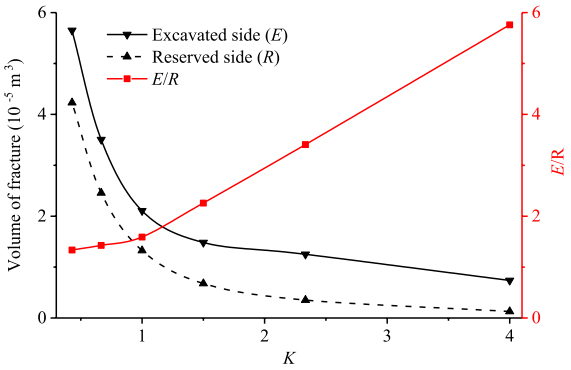

Fig. 13 Variations of fracture volume and *E*/*R* vs. *K*

increase of *K*. Hence, a large *K* is recommended to be adopted in air–water coupling blasting for controlling crack growth.

5.2 Effects of decoupling ratio

To investigate the effects of decoupling coefficient K_d on fracture control, the air–water coupling blasts with K_d=5.5, 5.0, 4.5, 4.0, and 3.5 are simulated with K=1. The obtained fracture patterns at the top and bottom surfaces are shown in Fig. 14. It can be observed that with different K_d, the extent of rock fracture in excavation rock is larger than that in the remaining rock on the whole, which again suggests that the fracture development is reasonably controlled in air–water coupling blasting. Besides, when the K_d reduces, the crushed zone gradually expands, and the blast-induced radial cracks become denser and longer due to the increased explosion energy. Consequently, similar to the decrease of *K*, the decrease of K_d leads to more severe damage to the reserved rock because of abundant explosion energy.

Figure 15 shows the variations in crack volume and *E*/*R* vs. K_d. As can be seen, the crack volumes on both sides of the excavation boundary reduce with the increase of K_d. Besides, the curve of *E*/*R* rises first, then descends and reaches its peak at K_d=4.0. This might be attributed to the mixing of air and water during blasting. When the charge radius is small, i.e. with a large K_d, the coupling mediums have a relatively large thickness, and thus the air and water thoroughly mix under blast loading. Thus, in air–water coupling blasting with a large K_d, the explosion energy transmits into rock through the air–water mixture, resulting in a relatively symmetric fracture distribution. With the charge radius increase i.e. with the K_d decrease, the mixing of air and water gradually weakens due to the small thickness of the coupling material. Under this condition, the explosion energy travels into the excavation rock and the remaining rock through water and air, respectively, and therefore the anisotropy of rock cracking becomes distinct.

However, when the charge radius continuously increases, as shown in the theoretical results in Fig. 2, the transfer efficiencies of explosion stress into rock through air and water are gradually approximate because of the thin coupling medium. Therefore, the crack distribution induced by air–water coupling blasting becomes symmetric again. Consequently, with the charge radius increase, the fracture control performance in air–water coupling blasting gets better as the K_d decreases from 5.86 to 4.0. Thereafter, it becomes worse as K_d changes from 4.0 to 3.5. This indicates that the best performance of fracture control in air–water coupling blasting is obtained when K_d=4.0. Hence, K_d=4.0 is recommended for blasting with air–water coupling to control crack development.

6 Concluding remarks

The present study proposes a new method of fracture control blasting using air–water coupling that aims to control the development of blast-induced fracture towards the excavation rock while protecting the remaining rock from damage. Furthermore, its performance is theoretically and numerically investigated. According to the current findings, some main conclusions can be summarized as follows:

1. During the air–water coupling blasting, the rock on the water-coupling side experiences much higher explosion stress, and thus the blast-induced fractures preferably propagate towards the excavation zone. In contrast, low explosion stress is transmitted into the rock on the air-cou-

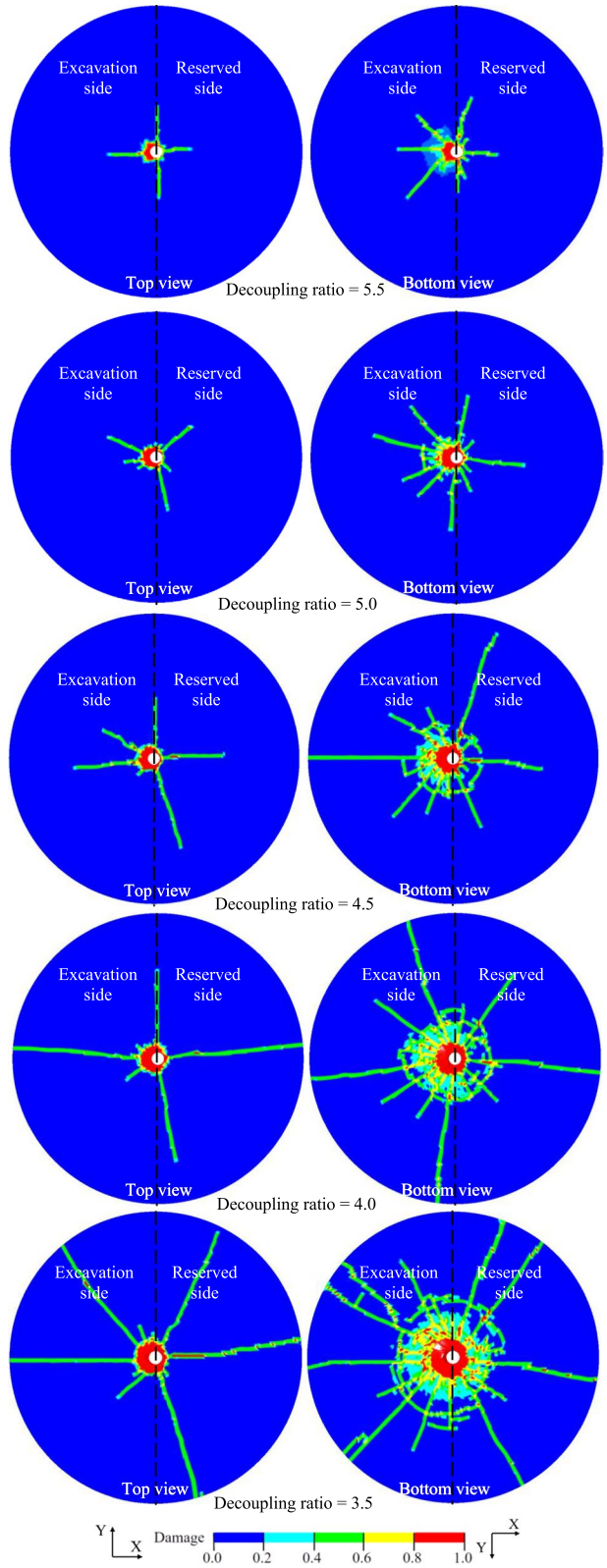

Fig. 14 Crack patterns induced by water–air coupling blasting with various K_d

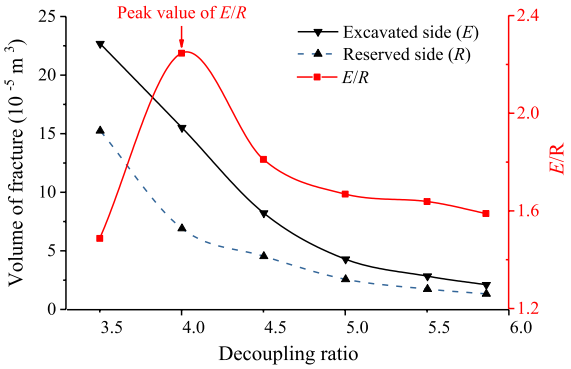

Fig. 15 Variations of fracture volume and E/R versus K_d

pling side, and therefore fewer and shorter cracks are created in the reserved rock. Meanwhile, the utilization efficiency of explosion energy in rock on the water-coupling side is higher than on the air-coupling side. In this way, good performance of fracture control is achieved under air–water coupling blasting.

2. The explosion stress field in rock gets stronger along the borehole axil at a distance from the initiation point due to the superposition of stress waves from explosive detonation at different locations, resulting in denser and longer fractures with distance from the detonation point increase in the direction of borehole axial.
3. When the air–water ratio increases, the explosion energy transmitted into rock decreases and the fracture control performance in air–water coupling blasting becomes better. A small air–water ratio is conducive to fracture control under air–water coupling blasting.
4. As the decoupling ratio reduces, the performance of fracture control under air–water coupling blasting gets better and then becomes undesirable. With an air–water ratio of 1, the best performance of fracture control using air–water coupling blasting is obtained when the decoupling ratio is 4.0.

In the present study, fracture control blasting using air–water coupling is first conceptually proposed, and its performance is preliminarily studied using theoretical and numerical tools. The dynamic response of rock under air–water coupling blasting will be further experimentally investigated in subsequent work.

Acknowledgements The authors acknowledge the financial support from the National Natural Science Foundation of China under Grant no. 51974360 for carrying out this research work.

Declarations

Conflict of interest The authors have no conflicts of interest to declare that are relevant to the content of this article.

References

An HM, Liu HY, Han H, Xin Z, Wang XG (2017) Hybrid finite-discrete element modelling of dynamic fracture and resultant fragment casting and muck-piling by rock blast. Comput Geotech 81:322–345. https://doi.org/10.1016/j.compgeo.2016.09.007

Banadaki MMD (2010) Stress-wave induced fracture in rock due to explosive action. University of Toronto, Scarborough

Bjarnholt G, Holmberg R, Ouchterlong F (1983) A linear shaped charge system for contour blasting. In: Proceeding of 9th conference on explosives and blasting technique. Society of Explosives Engineers, Dallas

Borrvall T, Riedel W (2011) The RHT concrete model in LS-DYNA. In: Proceedings of The 8th European LS-DYNA user conference

Brannon RM, Leelavanichkul S (2009) Survey of four damage models for concrete. In: Sandia National Laboratories, pp 1–80

Cho SH, Nakamura Y, Mohanty B, Yang HS, Kaneko K (2008) Numerical study of fracture plane control in laboratory-scale blasting. Eng Fract Mech 75(13):3966–3984. https://doi.org/10.1016/j.engfracmech.2008.02.007

Cui ZD, Yuan L, Yan CL (2010) Water–silt composite blasting for tunneling. Int J Rock Mech Min Sci 47(6):1034–1037. https://doi.org/10.1016/j.ijrmms.2010.06.004

Dally JW, Fourhey W (1977) Fracture control in construction blasting. In: The 18th US symposium on rock mechanics (USRMS). One Petro

Foster CL (1905) A Treatise of Ore and Stone Minning. Charles Griffin & Company, London
Fourney WL (1983) Fracture control blasting. Springer, Vienna
Fourney WL, Dally JW, Holloway DC (1978) Controlled blasting with ligamented charge holders. Int J Rock Mech Min Sci 15(3):121–129. https://doi.org/10.1016/0148-9062(78)90006-2
He MC, Cao WF, Shan RL, Wang SL (2003) New blasting technology bilateral cumulative tensile explosion. Chin J Rock Mech Eng 22(12):2047–2051
Henrych J, Major R (1979) The dynamics of explosion and its use. Elsevier, Amsterdam
Himanshu VK, Mishra A, Vishwakarma AK, Roy M, Singh P (2022) Explicit dynamics based numerical simulation approach for assessment of impact of relief hole on blast induced deformation pattern in an underground face blast. Geomech Geophys Geo 8(1):1–18. https://doi.org/10.1007/s40948-021-00327-5
Hoek E, Brown ET (1980) Underground excavation in rock. The institute of mining and metallurgy. CRC Press, London
Huang BX, Li PF (2015) Experimental investigation on the basic law of the fracture spatial morphology for water pressure blasting in a drillhole under true triaxial stress. Rock Mech Rock Eng 48(4):699–1709
Hustrulid WA, Bullock RL (2001) Underground mining method. Society for Mining, Metallurgy, and Exploration, Inc. Littleton, Colorado, USA
Iqbal MJ (2004) Comparison of fracture toughness measurement techniques in brittle rocks. University of Toronto. Toronto, Canada
Jacquot RG, Steadman JW, Rhodine CN (1983) The Gaver–Stehfest algorithm for approximate inversion of Laplace transforms. IEEE Circ Syst Mag 5(1):4–8. https://doi.org/10.1109/MCAS.1983.6323897
Jang H, Handel D, Ko Y, Yang HS, Miedecke J (2018) Effects of water deck on rock blasting performance. Int J Rock Mech Min Sci 112:77–83. https://doi.org/10.1016/j.ijrmms.2018.09.006
Jiang LL (2010) Mechanism and application of directional fracture blasting with slotted cartridge. Dissertation, China University of Mining and Technology, Beijing
Kirsch EG (1898) Die Theorie der Elasitzitt und die Bedürfnisse der Festigkeitslehre. Z VDI. zeitschrift des vereines deutscher ingenieure
Langefors U, Kihlström B, Kenkyūjo KS (1963) The modern technique of rock blasting. Almquist and Wiksell, Stockholm
Lee EL, Hornig HC, Kury JW (1968) Adiabatic expansion of high explosive detonation products, UCRL-50422
Li XB (2014) Rock dynamics fundamentals and applications. Science Press, Bejing
Li XP, Huang JH, Luo Y, Chen PP (2017) A study of smooth wall blasting fracture mechanisms using the timing sequence control method. Int J Rock Mech Min Sci 92:1–8. https://doi.org/10.1016/j.ijrmms.2016.12.001
Li X, Xu M, Wang Y, Wang G, Huang J, Yin W, Yan G (2021a) Numerical study on crack propagation of rock mass using the time sequence controlled and notched blasting method. Eur J Environ Civ Eng. https://doi.org/10.1080/19648189.2021a.1956597
Li XH, Zhu ZM, Meng W, Wan DY, Zhou L, Liu RF (2021b) Numerical study on the behavior of blasting in deep rock masses. Tunn Undergr Space Technol 113:103968. https://doi.org/10.1016/j.tust.2021.103968
Li Y, Huang C, Liu L, Chen X, Zhao Q (2021c) Experimental and numerical investigation on the explosive characteristics of slotted cartridges under different slotted structures. Rock Mech Rock Eng. https://doi.org/10.1007/s00603-021-02592-y
Li X, Pan C, Li X, Shao C, Li H (2022a) Application of a synthetic rock mass approach to the simulation of blasting-induced crack propagation and coalescence in deep fractured rock. Geomech Geophys Geo 8(2):1–17. https://doi.org/10.1007/s40948-022-00376-4
Li XD, Liu KW, Yang JC, Song RT (2022b) Numerical study on blast-induced fragmentation in deep rock mass. Int J Impact Eng 170:104367. https://doi.org/10.1016/j.ijimpeng.2022b.104367
Li BH (2013) Research on theory and application technology of elliptic bipolar linear shaped charge's presplit blasting. Dissertation, Central South University
Liu KW, Yang JC, Li XB, Hao H, Li QY, Liu ZX, Wang CY (2018) Study on the long-hole raising technique using one blast based on vertical crater retreat multiple deck shots. Int J Rock Mech Min Sci 109:52–67. https://doi.org/10.1016/j.ijrmms.2018.06.020
Liu J, Guo X, Liu Z, Liu X, Liu Q (2019a) Pressure field investigation into oil&gas wellbore during perforating shaped charge explosion. J Petrol Sci Eng 172:1235–1247. https://doi.org/10.1016/j.petrol.2018.09.068
Liu KW, Li XD, Hao H, Li XB, Sha YY, Wang WH, Liu XL (2019b) Study on the raising technique using one blast based on the combination of long-hole presplitting and vertical crater retreat multiple-deck shots. Int J Rock Mech Min Sci 113:41–58. https://doi.org/10.1016/j.ijrmms.2018.11.012
LSTC (2015) LS-DYNA keyword user's manual, version R 8.0
Luo Y, Shen Z (2006) Study on orientation fracture blasting with shaped charge in rock. J Univ Sci Technol Beijing Min Metall Mater 13(3):193–198. https://doi.org/10.1016/S1005-8850(06)60042-X
Ma GW, An XM (2008) Numerical simulation of blasting-induced rock fractures. Int J Rock Mech Min Sci 45(6):966–975. https://doi.org/10.1016/j.ijrmms.2007.12.002
Martino JB, Chandler NA (2004) Excavation-induced damage studies at the underground research laboratory. Int J Rock Mech Min Sci 41(8):1413–1426. https://doi.org/10.1016/j.ijrmms.2004.09.010
Mckown AF (1986) Perimeter control blasting for underground excavations in fractured and weathered rock. Environ Eng Geosci 23(4):461–478. https://doi.org/10.2113/gseegeosci.xxiii.4.461
Miklowitz AJ (1978) The theory of elastic waves and waveguides. North-Holland Publishing Company, Amsterdam
Nakagawa K, Sakamoto T, Yoshikai R (1982) Model study of the guide hole effect on the smooth blasting. J Jpn Exp Soc 43:75–82
Nakamura Y (1999) Model experiments on effectiveness of fracture plane control methods in blasting. Fragblast 3(1):59–78. https://doi.org/10.1080/13855149909408034

Nakamura Y, Matsunaga H, Yamamoto M, Sumiyoshi K (1992) Blasting methods for crack control by utilizing charge holders. Kogyo Kayaku 53(1):31–37

Pan C, Xie LX, Li X, Liu K, Gao PF, Tian LG (2022) Numerical investigation of effect of eccentric decoupled charge structure on blasting-induced rock damage. J Cent South Univ 29:663–679. https://doi.org/10.1007/s11771-022-4947-3

Riedel W, Kawai N, Kondo KI (2009) Numerical assessment for impact strength measurements in concrete materials. Int J Impact Eng 36(2):283–293. https://doi.org/10.1016/j.ijimpeng.2007.12.012

Riedel W, Thoma K, Hiermaier S, Schmolinske E (1999) Penetration of reinforced concrete by BETA-B-500 numerical analysis using a new macroscopic concrete model for hydrocodes. In: Proceedings of the 9th international symposium on the effects of munitions with structures. Berlin-Strausberg, Germany

Sanchidrián JA, García-Bermudez P, Jimeno CL (2000) Optimization of granite splitting by blasting using notched holes. Fragblast 4(1):1–11. https://doi.org/10.1080/13855140009408059

Shu YR, Ran ZZ, Yun YL, Xian GY (2013) Cumulative blasting experiment study of slotted cartridge based on hard-rock rapid driving technology. Chin J Rock Mech Eng 32(2):317–323

Shu YR, Long CY, Kai FD, Xun WQ (2014) Tests for blasting vibration reduction technique with presplitting blasting of a slotted cartridge. J Vib Shock 33(12):7–14 (**[in Chinese]**)

Singh PK, Roy MP, Paswan RK (2014) Controlled blasting for long term stability of pit-walls. Int J Rock Mech Min Sci 70:388–399. https://doi.org/10.1016/j.ijrmms.2014.05.006

Sun Y, Bi R, Sun J, Zhang J, Taherdangkoo R, Huang J, Li G (2022) Stability of roadway along hard roof goaf by stress relief technique in deep mines: a theoretical, numerical and field study. Geomech Geophys Geo 8(2):1–16. https://doi.org/10.1007/s40948-022-00356-8

Thompson D, McKown A, Fourney W, Sperry P (1979) Field evaluation of fracture control in tunnel blasting. No. DOT-TSC-UMTA-79–44 Final Rpt.

Tsoutrelis C, Gikas N, Nomikos P, Exadaktylos G (1997) Use of notched boreholes for fracture controlled blasting in the ornamental stone quarries. Fragblast 1(4):445–463. https://doi.org/10.1080/13855149709408408

Verma HK, Samadhiya NK, Singh M, Goel RK, Singh PK (2018) Blast induced rock mass damage around tunnels. Tunn Undergr Space Technol 71:149–158. https://doi.org/10.1016/j.tust.2017.08.019

Wang YB (2017) Study of the dynamic fracture effect using slotted cartridge decoupling charge blasting. Int J Rock Mech Min Sci 96:34–46. https://doi.org/10.1016/j.ijrmms.2017.04.015

Wang Q, Wang Y, He M, Li S, Jiang Z, Jiang B, Xu S, Wei H (2022) Experimental study on the mechanism of pressure releasing control in deep coal mine roadways located in faulted zone. Geomech Geophys Geo 8(2):1–24. https://doi.org/10.1007/s40948-021-00337-3

Wei XY, Zhao ZY, Gu J (2009) Numerical simulations of rock mass damage induced by underground explosion. Int J Rock Mech Min Sci 46(7):1206–1213

Xie LX, Lu WB, Zhang QB, Jiang QH, Chen M, Zhao J (2017) Analysis of damage mechanisms and optimization of cut blasting design under high in-situ stresses. Tunn Undergr Space Technol 66:19–33. https://doi.org/10.1016/j.tust.2017.03.009

Yan SL, Xu Y (2005) Numerical simulation of water-coupled charge rock blasting mechanism. Chin J Undergr Space Eng 1(6):921–924

Yan P, Lu WB, Chen M, Hu YG, Zhou CB, Wu XX (2015) Contributions of in-situ stress transient redistribution to blasting excavation damage zone of deep tunnels. Rock Mech Rock Eng 48(2):715–726. https://doi.org/10.1007/s00603-014-0571-3

Yang Y, Li X, Ju Y (2022) Influence mechanisms of plasticity and horizontal stress difference on the fracture propagation in plastic reservoir rocks: a 3D XFEM-based plastic fracturing model. Geomech Geophys Geo 8(5):1–19. https://doi.org/10.1007/s40948-022-00453-8

Yi CP, Johansson D, Greberg J (2017) Effects of in-situ stresses on the fracturing of rock by blasting. Comput Geotech. https://doi.org/10.1016/j.compgeo.2017.12.004

Yin Y, Sun Q, Zou B, Mu Q (2021) Numerical study on an innovative shaped charge approach of rock blasting and the timing sequence effect in microsecond magnitude. Rock Mech Rock Eng. https://doi.org/10.1007/s00603-021-02516-w

Yu MH (1998) Twin Shear Theory and its Application. Science Press, Beijing

Yuan W, Wang W, Su XB, Wen L, Chang JF (2019) Experimental and numerical study on the effect of water-decoupling charge structure on the attenuation of blasting stress. Int J Rock Mech Min Sci 124:104133. https://doi.org/10.1016/j.ijrmms.2019.104133

Zhang QB, Zhao J (2014) A review of dynamic experimental techniques and mechanical behaviour of rock materials. Rock Mech Rock Eng 47(4):1411–1478. https://doi.org/10.1007/s00603-013-0463-y

Zhang Q, Li XB, Zhu FC (1998) Stress and energy transfer of water coupling blasting. Trans Nonferr Metal Soc 8(2):342–248

Zhang AM, Yang WS, Yao XL (2012) Numerical simulation of underwater contact explosion. Appl Ocean Res 34:10–20. https://doi.org/10.1016/j.apor.2011.07.009

Zhang S, Wang G, Chao W, Pang B, Du C (2014) Numerical simulation of failure modes of concrete gravity dams subjected to underwater explosion. Eng Fail Anal 36(1):49–64. https://doi.org/10.1016/j.engfailanal.2013.10.001

Zhang XY, Hu JZ, Xie HJ, Mao WB, Gao YB, Yang J, He MC (2020) Innovative approach based on roof cutting by energy-gathering blasting for protecting roadways in coal mines. Tunn Undergr Space Technol. https://doi.org/10.1016/j.tust.2020.103387

Zou DX (2017) Theory and technology of rock excavation for civil engineering. Springer, Singapore